Spring 5-15-2020

Application of Photoacoustic Imaging in Understanding Tissue Remodeling

Yuan Qu
Washington University in St. Louis

Recommended Citation

Qu, Yuan, "Application of Photoacoustic Imaging in Understanding Tissue Remodeling" (2020). *McKelvey School of Engineering Theses & Dissertations*. 550.
https://openscholarship.wustl.edu/eng_etds/550

WASHINGTON UNIVERSITY IN ST. LOUIS

McKelvey School of Engineering
Department of Biomedical Engineering

Dissertation Examination Committee:
Dr. Lihong Wang, Co-Chair
Dr. Yong Wang, Co-Chair
Dr. Molly J. Stout
Dr. Methodius G. Tuuli
Dr. Chao Zhou
Dr. Quing Zhu

Application of Photoacoustic Imaging in Understanding Tissue Remodeling

by
Yuan Qu

A dissertation presented to
The Graduate School
of Washington University in
partial fulfillment of the
requirements for the degree
of Doctor of Philosophy

May 2020
St. Louis, Missouri

Table of Contents

List of Figures

List of Tables

Acknowledgments

I would like to start by thanking my Ph.D. advisors, Dr. Lihong Wang, Dr. Methodius Tuuli, and Dr. Molly J. Stout, for all their support. I have benefited enormously from their supervision. I also appreciate my other committee members, Dr. Mark Anastasio, Dr. Yong Wang, Dr. Quing Zhu, and Dr. Chao Zhou, for their support. I want to thank all the members of the March of Dimes Prematurity Research Center for many enlightening discussions and good memories. In particular, I would like to thank Dr. Konstantin I. Maslov, Dr. Chiye Li, Dr. Junhui Shi, Dr. Peinan Zhao, Dr. Thomas Matthews, and Dr. Yang Lou, who helped get me through numerous difficulties in my PhD program.

I would also like to thank the staff at Washington University in St. Louis, such as James Ballard, Cynthia Goessling, Susan Seel, Karen Teasdale, and Dr. Jin-Yu Shao, just to name a few. I am especially indebted to them for their enthusiastic support in my student affairs.

I would like to thank the March of Dimes for the funding support.

Finally, I would like to thank my parents for their love and support.

Yuan Qu

Washington University in St. Louis

May 2020

ABSTRACT OF THE DISSERTATION

Application of Photoacoustic Imaging in Understanding Connective Tissue Remodeling

by

Yuan Qu

Doctor of Philosophy in Biomedical Engineering

Washington University in St. Louis, 2020

Professor Lihong Wang, Co-Chair

Professor Yong Wang, Co-Chair

Photoacoustic Imaging (PAI) as an imaging method in biomedical research can provide high spatial resolution, various contrasts, great detection sensitivity, and deep penetration. These advantages are attributed to the combination of optical excitation and acoustic detection, which releases PAI from the ballistic limit faced by other optical imaging technique with high spatial resolution. In this dissertation, we aim to apply this technique to understand the connective tissue remodeling that is a ubiquitous physiological change in various medical complications.

Chapter 1 elaborates the mechanism of PAI as well as the motivation of my dissertation.

In Chapter 2, I introduce a new contrast mechanism for PAI, developed during this research. This contrast mechanism enables PAI to image the alignment of collagen fibers that make up connective tissue. Furthermore, the novel imaging method can measure both the amplitude of tissue's dichroism and the orientation of the optic axis of uniaxial dichroic tissue. I experimentally demonstrate the performance of this method by imaging *ex vivo* connective tissue inside scattering media and successfully detect the orientation of the optic axis of uniaxial dichroic materials beyond

the ballistic limit. The results show that the proposed method will extend the capability of PAI to imaging tissue absorption anisotropy.

Chapter 3 describes the development of a transvaginal acoustic-resolution photoacoustic endoscope. The endoscope is 20 mm in diameter, rigid, and side-scanning. The scan is driven by a servo motor which provides a 10 Hz B-scan frame rate with a 30° scanning angle. I demonstrate the performance in phantom, *ex vivo*, and *in vivo* experiments. This device will be useful for monitoring physiological change associated with variation of blood oxygenation.

Chapter 4 introduces a new method to quantify tissue hydration by measuring near-infrared spectra. I first demonstrate this method in hydrogel phantoms as an analog of connective tissue. Then, I apply this method to pregnant women *in vivo*, and observe an increase in the water content of the cervix throughout pregnancy. The application of this technique in healthcare may advance our understanding of connective tissue remodeling.

Chapter 5 presents a transvaginal fast-scanning optical-resolution photoacoustic endoscope with a 250 Hz B-scan rate over a 3 mm scanning range. Using this modality, I not only illustrate the morphological differences of vasculatures among human tissues, but also show the longitudinal and cross-sectional differences of cervical vasculatures in pregnant women. This technology is promising for screening the visceral pathological changes associated with angiogenesis.

In chapter 6, I show how the tissue oxygenation, hydration, and vascularity change with cervical remodeling through pregnancy. In the study, I observe an overall increase of tissue hydration. In contrast, the tissue oxygenation does not change much. As future work, a systematic study illustrating the role of cervical remodeling in complications of preterm labor should focus on high-risk populations.

Chapter 1: Introduction

1.1 Photoacoustic Tomography

In the life sciences, imaging illuminates biological mechanisms from molecular to anatomical levels. At the molecular level, optical microscopy can illustrate complicated genome conformations [1] and subcellular skeletal structures [2], as well as the associated molecular transports [3]. At the anatomical level, positron emission tomography and single-photon emission computed tomography achieve high sensitivity and specificity by labeling receptors with radioactive molecular probes. X-ray computed tomography, magnetic resonance imaging, and ultrasound imaging can visualize the anatomy without labeling [4]. In general, the capability of the foregoing imaging modalities is constrained at either the molecular level or the anatomical level by their imaging contrast mechanisms. However, photoacoustic tomography (PAT) is an exception: this special technology can image substances and structures from microscopic to macroscopic scales.

PAT can image across multiple scales by acoustically detecting optical absorption contrast via the photoacoustic (PA) effect, in which a laser pulse targeting one molecular characteristic absorption band is converted into an ultrasonic wave freely propagating in an optically scattering medium. This combination offers three advantages. First, PAT can provide anatomical and functional imaging through endogenous contrast and for molecular and provide cellular imaging through exogenous contrasts [5, 6]. Second, PAT's scalable spatial resolution can go beyond the ballistic regime that constrains optical microscopy, but still provide optical contrast [5]. Third, PAT is complementary to and compatible with other imaging modalities, augmenting their imaging capability by adding more anatomic and functional information [6].

With these advantages, PAT can be implemented in two major forms [5]. The first form, photoacoustic microscopy (PAM), detects the photoacoustic (PA) signal excited by one laser pulse at a single spot and scans the spot across the entire field of view (FOV) with repeated excitations. We can classify PAM into two categories, optical-resolution PAM (OR-PAM) and acoustic-resolution PAM (AR-PAM). OR-PAM detects the PA signal excited by a focused laser beam and has an optical diffraction-limited lateral resolution, typically ~ 3 µm. AR-PAM, to achieve a larger imaging depth than OR-PAM, detects the PA signal excited by diffused light and its lateral resolution depends on the size of the acoustic focus, typically ~ 40 µm. The second form, photoacoustic computed tomography (PACT), can be implemented by a transducer array, and the resolution in the imaging plane is ~ 100 µm.

1.2 Motivation

This dissertation enriches our knowledge of connective tissue remodeling, which is a pivotal biological mechanism involved in parturition [7], wound healing, fibrotic diseases [8], and tumor invasion [9]. First, we demonstrate a new contrast mechanism that enables PAT to image collagen fibers (Chapter 2), the building blocks of connective tissue. Second, we develop an endoscope that can quantify oxygenation in connective tissue (Chapter 3). Many physiological processes are associated with oxygen consumption, and connective tissue remodeling may be among these processes. Third, we use near-infrared spectroscopy to illuminate the relation between connective tissue remodeling and change of tissue hydration (Chapter 4). Fourth, we implement *in vivo*, noninvasive angiography with capillary-level spatial resolution (Chapter 5), to validate the hypothesis that angiogenesis accompanies the changes of extracellular matrix [10]. In the end, we combine the information acquired by different devices to show how tissue changes during cervical remodeling in pregnancy (Chapter 6).

Chapter 2: Dichroism-sensitive Photoacoustic Tomography

This chapter describes a new contrast mechanism for photoacoustic tomography, which used to image the spatial distribution of optical absorption and regard the absorption coefficient as a scalar. In fact, the absorption coefficients of many biological tissues exhibit an anisotropic property, known as dichroism, which depends on molecular conformation and structural alignment. Here, I present a novel imaging method called dichroism-sensitive photoacoustic computed tomography (DS-PACT), which measures both the amplitude of tissue's dichroism and the orientation of the optic axis of uniaxial dichroic tissue. By modulating the polarization of linearly polarized light and measuring the alternating signals through lock-in detection, DS-PACT can boost dichroic signals from biological tissues.

2.1 Background

Medical imaging using non-ionizing radiation can discover and monitor diseases without hazard to the human body [11, 12]. Photoacoustic (PA) tomography (PAT) combines non-ionizing photons and low-scattering ultrasound to achieve high optical contrast and high spatial resolution imaging at depths beyond the optical diffusion limit, given by the transport mean free path [13–15]. Nevertheless, conventional PAT commonly treats the absorption coefficient as a scalar variable, which does not take the absorption anisotropy of biological tissue into consideration. In practice, however, many biological tissues exhibit dichroism, which means photons in different polarization states traveling through the tissue experience different degrees of absorption.

Dichroism is related to molecular conformation and structural alignment. For example, amyloid, a hallmark of a wide spectrum of protein aggregation disorders, is dichroic [16]. Because PAT converts a small fractional change in the optical absorption coefficient to an equal fractional change in the PA signal, the ratio of the latter to the former, defined as the relative sensitivity to optical absorption, is 100%. Thus, it could be an ideal modality to study the dichroism of biological tissues. Very recently, PA microscopy with optical resolution has demonstrated its capability to image dichroism [16]. However, the demonstrated depth is within the ballistic regime, which is too shallow for many preclinical and clinical applications.

PA computed tomography (PACT) is an embodiment of PAT that provides up to multiple centimeters' imaging depth in tissues with high spatial resolution [17–20]. Here, we present a new approach, called dichroism-sensitive PACT (DS-PACT), which we developed by upgrading a conventional PACT system [21] for dichroism measurement. Benefiting from the deep penetration of PACT, the new approach can image the dichroism of biological tissue at depths beyond the transport mean free path. Moreover, by modulating the polarization of linearly polarized light and measuring the alternating signals through lock-in detection [22], DS-PACT can significantly enhance the imaging contrast among biological tissues with different dichroism, and can also image the orientation of the optic axis of uniaxial dichroic tissue. We first investigated the principle of our approach, then we demonstrated it by imaging the dichroism of both plastic polarizers and biological tissues (bovine tendon) buried deep inside scattering media.

2.2 Methods

The PACT system used in this study (Figure 2.1) was upgraded from that in our previous work [21]. A frequency-doubled Nd:YAG laser (LS-2137, LOTIS) at 532 nm with a 10 Hz pulse repetition rate was used for excitation. The output laser beam was vertically polarized. A half-wave plate was used to rotate the polarization of the linearly polarized laser beam. A stepper motor triggered by a function generator rotated the half-wave plate so that the polarization angle of the excitation light before entering the scattering medium was rotated with a period of 32.00 s (corresponding to a rotation frequency $f_M = 0.03125\,\text{Hz}$). A concave lens then expanded the incident light to a diameter of ~2.5 cm on the sample surface. The maximum light fluence on the surface of our sample was ~15 mJ/cm^2, within the American National Standards Institute safe exposure limit [23].

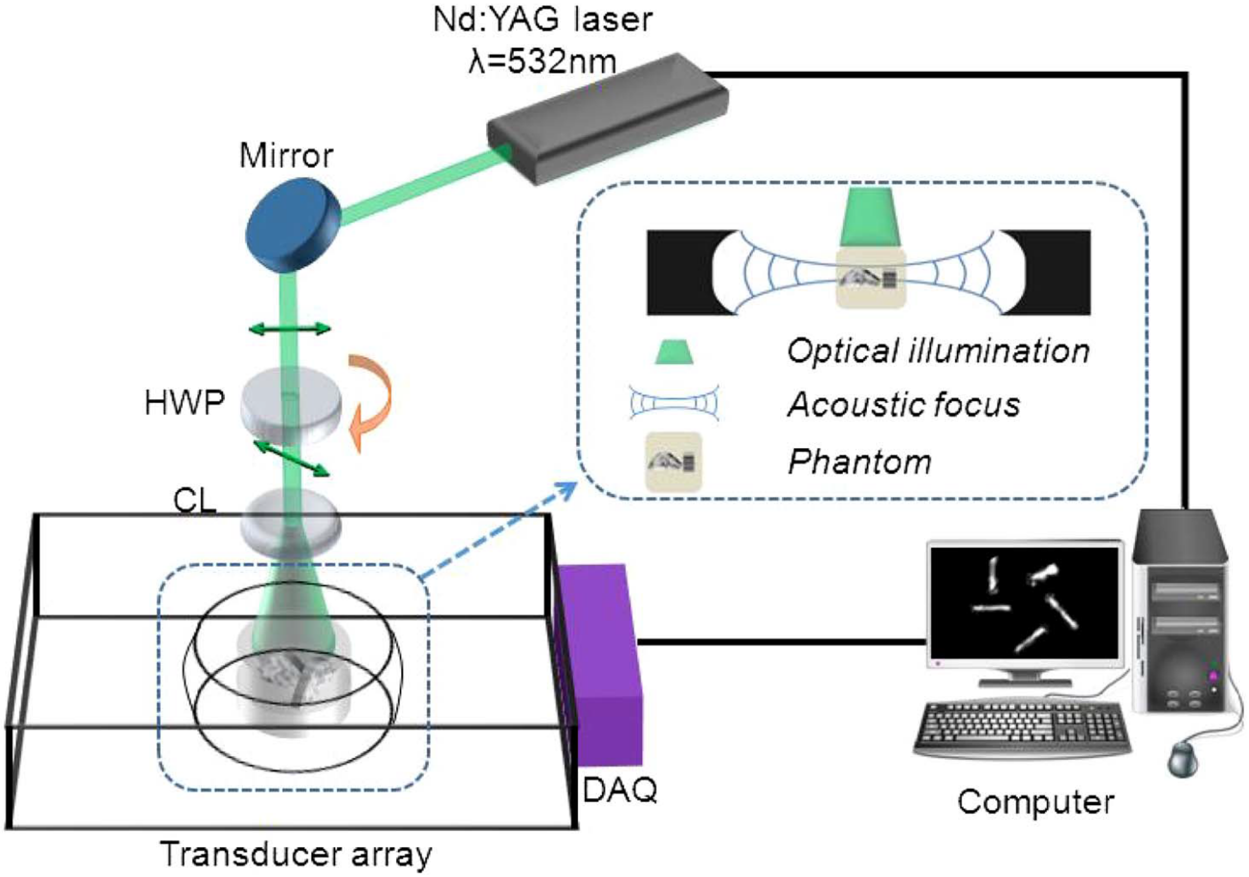

Figure 2.1 Experimental setup of DS-PACT. The polarization of linearly polarized light is modulated by a half-wave plate, which is driven by a stepper motor. The light is then expanded by a concave lens. HWP, half-wave plate; CL, concave lens; DAQ, data acquisition system.

While illuminating the sample with polarization-rotated light, we collected a sequence of conventional PACT images. The PA signals were detected by a full-ring ultrasonic transducer array with a 5 cm diameter (Imasonic, 5 MHz central frequency, more than 80% one-way bandwidth, and 512 elements). Each element (10 mm high, 0.3 mm pitch, and 0.1 mm inter-element space) was arc-shaped to produce an axial focal distance of 19.8 mm in the imaging plane. The imaging region at the center of the full-ring transducer array consisted of the foci of all 512 elements, and was approximately 20 mm in diameter and 1 mm in thickness. The in-plane resolution was quantified as ~100 μm [21]. The data acquisition system had 64 channels, with eight-fold multiplexing. The cross-sectional imaging speed was 1.6 s per frame. To address the acoustic inhomogeneity between the dichroic materials (DMs) and medium, the half-time image reconstruction was applied in combination with the universal back-projection reconstruction algorithm [24].

Unless otherwise stated, the DMs were embedded in agar gels (3% agar in distilled water). To introduce scattering, on top of the gel, we stacked an additional layer of a scattering medium (0.25% Intralipid and 3% agar in distilled water, with a reduced scattering coefficient of ~0.25 mm^{-1} and a transport mean free path of ~4 mm). By varying the thicknesses of the scattering layer from 0 mm (no scattering medium) to 20 mm, we quantified the system performance at different depths.

Here, we describe the operating principle of DS-PACT. When the excitation light has a polarization angle ϕ, the PA amplitude $PA(\vec{r},\phi)$ defined in the imaging plane is a function of both the spatial position $\vec{r}$ and the polarization angle ϕ. Mathematically, $PA(\vec{r},\phi)$ can be represented as the product of the optical absorption coefficient $\mu_a(\vec{r},\phi)$ of the biological tissue and the local light fluence $F(\vec{r},\phi)$ [25]:

$$PA(\vec{r},\phi) \propto \mu_a(\vec{r},\phi)F(\vec{r},\phi) \tag{2.1}$$

In our study, the DMs are assumed to be uniaxial. Thus, the absorption coefficient $\mu_a(\vec{r},\phi)$ in Equation (2.1) along the polarization direction is [26]

$$\mu_a(\vec{r},\phi) = \mu_{a,o}(\vec{r})\frac{n^3(\vec{r},\phi)}{n_o^3(\vec{r})}\cos^2(\phi-\theta(\vec{r})) + \mu_{a,e}(\vec{r})\frac{n^3(\vec{r},\phi)}{n_e^3(\vec{r})}\sin^2(\phi-\theta(\vec{r})) \tag{2.2}$$

Here, $\theta(\vec{r})$ is the orientation of the optic axis of the biological tissue at the position $\vec{r}$. $n(\vec{r},\phi)$, $n_o(\vec{r})$ and $n_e(\vec{r})$, accounting for the refraction, are, respectively, the spatial distributions of the real part of the refractive index along the polarization direction, the direction perpendicular to the optic axis, and the direction parallel to the optic axis. $\mu_{a,o}(\vec{r})$ and $\mu_{a,e}(\vec{r})$ are the spatial distributions of the absorption coefficient perpendicular and parallel to the optic axis, respectively. The subscripts *o* and *e* stand for the words "ordinary" and "extraordinary." For many anisotropic tissues, such as tendon, the fractional change of the refractive index $\Delta n/\bar{n} = (n_o - n_e)/\left(\frac{n_o+n_e}{2}\right)$ is on the order of 10^{-4} [27]. Therefore, we assume here that $n(\vec{r},\phi) \approx n_o(\vec{r}) \approx n_e(\vec{r})$ and reduce Equation (2.2) as follows:

$$\begin{aligned}\mu_a(\vec{r},\phi) &\approx \mu_{a,o}(\vec{r})\cos^2\big(\phi-\theta(\vec{r})\big) + \mu_{a,e}(\vec{r})\sin^2\big(\phi-\theta(\vec{r})\big),\\ &= \frac{\mu_{a,o}(\vec{r})+\mu_{a,e}(\vec{r})}{2} + \frac{\mu_{a,o}(\vec{r})-\mu_{a,e}(\vec{r})}{2}\cos 2\big(\phi-\theta(\vec{r})\big),\\ &= \bar{\mu}_a(\vec{r})\left[1+\frac{\Delta\mu_a(\vec{r})}{2\bar{\mu}_a(\vec{r})}\cos 2\big(\phi-\theta(\vec{r})\big)\right],\end{aligned} \tag{2.3}$$

where $\Delta\mu_a(\vec{r}) = \mu_{a,o}(\vec{r}) - \mu_{a,e}(\vec{r})$ and $\bar{\mu}_a(\vec{r}) = \frac{\mu_{a,o}(\vec{r})+\mu_{a,e}(\vec{r})}{2}$, respectively, are the variation and the average of the absorption coefficient. For tendon, $\Delta\mu_a(\vec{r})/2\bar{\mu}_a(\vec{r})$ can be as high as 0.2 [27], and thus induces easily detectable changes in the PA amplitude.

Because the fractional change of the refractive index is on the order of 10^{-4}, we approximate $F(\vec{r},\phi)$ to $F(\vec{r})$. Providing that ϕ is rotated with a frequency of f_M, Equation (2.1) can be rewritten as

$$PA(\vec{r},\phi) \propto F(\vec{r})\bar{\mu}_a(\vec{r})\left[1 + \frac{\Delta\mu_a(\vec{r})}{2\bar{\mu}_a(\vec{r})}\cos 2\big(2\pi f_M t - \theta(\vec{r})\big)\right]. \qquad (2.4)$$

As we can see from Equation (2.4), the PA amplitude oscillates at a frequency of $2f_M$. Here we notice that the initial phase, $2\theta(\vec{r})$, is twice the orientation angle of the optic axis.

Figure 2.2 is a schematic of the image reconstruction process of DS-PACT. First, as shown in Fig. 2.2(a), a sequence of conventional PACT images is acquired at a frame rate of 0.625 Hz. The polarization of the incident light is rotated at 11.25°/s. Figure 2.2(b) then plots the PA amplitude

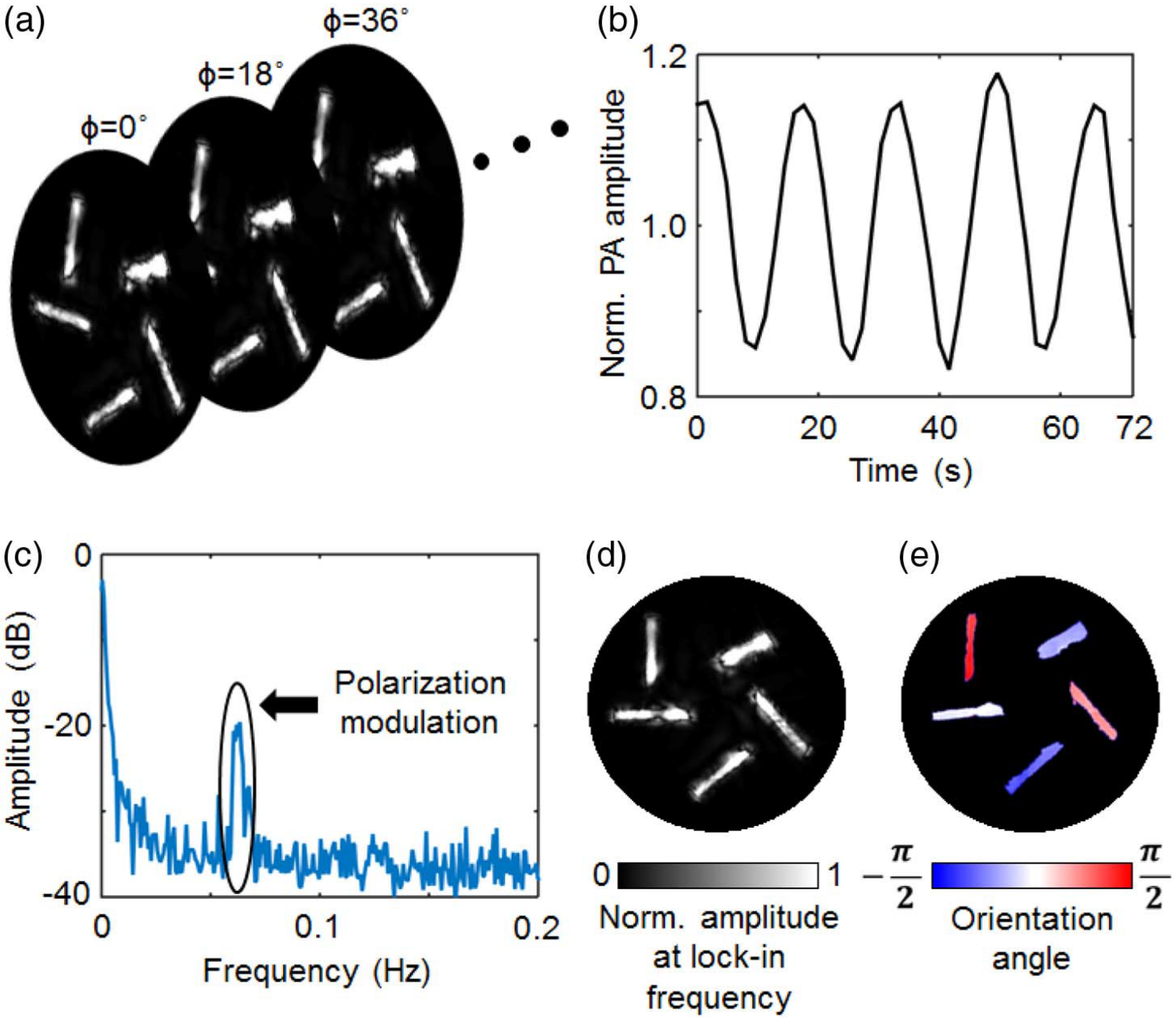

Figure 2.2 Schematic of image reconstruction. (a) A sequence of conventional PACT images is acquired at a frame rate of 0.625 Hz, rotating the polarization of the incident light at 11.25°/s. (b) Normalized PA amplitude as a function of time at one representative spatial point. *PA*(*t*) is normalized with respect to its average. (c) Fourier spectrum of *PA*(*t*). The peak located at 0.0625 Hz corresponds to the alternating PA signals due to the modulated polarization. (d) DS-PACT image reconstructed by the amplitude of the lock-in term in Equation (2.4). (e) Color-coded

orientation angle map of the sample, which is reconstructed from the phase of the lock-in term in Equation (2.4).

at one representative spatial position along the time sequence. As shown in Fig. 2.2(b), the PA amplitude oscillates with a period of 16 s, which corresponds to the frequency of $2f_M = 0.0625$ Hz from Equation (2.4). The Fourier transform of the time sequence in Fig. 2.2(b) is shown in amplitude in Fig. 2.2(c). The direct current term at zero frequency corresponds to $F(\vec{r})\bar{\mu}_a(\vec{r})$ in Equation (2.4), while the peak located at the frequency of 0.0625 Hz corresponds to the alternating current term in Eq. (4), and we will lock in to this term. By calculating the Fourier transform of the PA amplitude from the sequence of reconstructed conventional PACT images [Fig. 2.2(a)] pixel by pixel (over the entire field of view), we can obtain images representing the amplitude of dichroism and the initial orientation angle of the optic axis. A reconstructed image based on the amplitude of dichroism is shown in Fig. 2.2(d). The reconstructed image that denotes the orientation angle $\theta(\vec{r})$ of the optic axis of the DM is shown in Fig. 2(e). To highlight the DMs in Fig. 2.2(e), the orientation information is shown only at positions where the corresponding PA amplitudes are above a certain threshold value. In our work, the threshold was set at four times the noise level in the conventional PACT images, where the noise level was estimated as the standard deviation of the background signal outside the object region. We also emphasize here that DS-PACT has the potential to detect dichroism deep inside scattering media. The lock-in detection strategy can theoretically scale the signal-to-noise ratio (SNR) with the number of frames N as $\sqrt{N}$ [28], so that we can detect a weak response to polarization below a thick scattering medium by increasing N.

2.3 Results

Phantom Experiment

Having demonstrated the operating principle, we now quantify the performance of DS-PACT by imaging the dichroism of linear polarizers. The sample was made by embedding two plastic linear polarizers and two pieces of silicone rubber in the agar medium [Fig. 2.3(a)]. Then 900 conventional PACT images spanning 90 modulation cycles were collected. In the reconstructed conventional PACT image [Fig. 2.3(b)], both the linear polarizers and silicone rubber can be visualized. The PA amplitude ratio of the linear polarizers to the silicone rubber was approximately

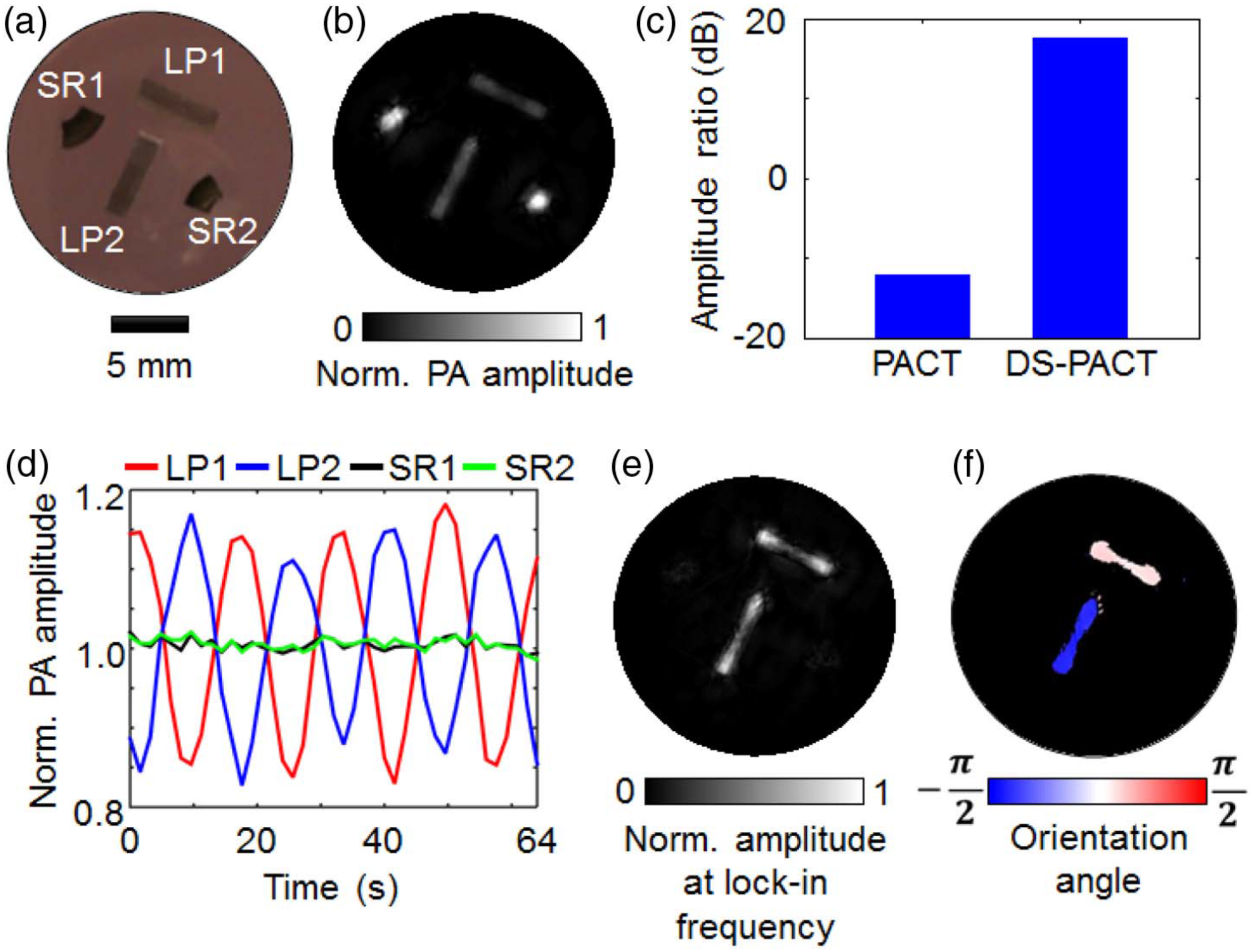

Figure 2.3 DS-PACT of linear polarizers and silicone rubber. (a) Photograph of the sample without any scattering medium. LP, linear polarizer; SR, silicone rubber. (b) Conventional PACT image averaged over 900 frames. (c) Amplitude ratio of the linear polarizers to the silicone rubber in the conventional PACT image and in the DS-PACT image. (d) Normalized PA amplitudes of the linear polarizers and silicone rubber. (e) DS-PACT image reconstructed by the amplitude of the lock-in term in Eq. (2.4). (f) Orientation angle map of the linear polarizers, in which two pieces of silicone rubber are not shown.

equal to −12.04 dB [Fig. 2.3(c)]. Although the silicone rubber has a PA amplitude that is four times the value of the linear polarizer, the PA amplitude of the silicone rubber did not vary with the modulated polarization of the excitation light. In contrast, the PA amplitudes of the linear polarizers were modulated by the polarization of the excitation light. Figure 2.3(d) shows the PA amplitudes of these four objects. As we can see from the figure, the PA amplitudes of the two linear polarizers have a π phase shift, because their optic axes are mutually perpendicular. The reconstructed DS-PACT images are shown in Figs. 2.3(e) and 2.3(f). Figure 2.3(e) is the DS-PACT image, reconstructed by the amplitude of the lock-in term in Eq. (2.4) and highlighting the spatial distribution of the linear polarizers. In this image, the silicone rubber is much less prominent than the linear polarizers because their PA amplitudes are not modulated by the polarization. The temporal-frequency amplitude ratio at $2f_M$ of the linear polarizers to the silicone rubber was approximately 17.58 dB [Fig. 2.3(c)]. Figure 2.3(f) is a color-coded orientation angle map of the linear polarizers, reconstructed from the phase of the lock-in term in Eq. (2.4). Therefore, unlike conventional PACT, DS-PACT can highlight the materials with dichroism and detect the orientations of their optic axes, while suppressing the materials without dichroism. These results are consistent with our hypotheses, supporting the operating principle.

Light gradually loses its original polarization when propagating deeper and deeper in a scattering medium. As a result, the amplitude of the lock-in term gradually decreases and is finally overwhelmed by noise. Therefore, to investigate the performance of DS-PACT at different depths in scattering media, we embedded five linear polarizers at different orientations in the agar medium [Fig. 2.4(a)] and varied the thickness of the scattering layer above. We analyzed the modulation depth $\Delta PA(D)$ as a function of the thickness D of the scattering medium. Here, $\Delta PA(D)$ is defined as the difference between the maximum PA amplitude and the minimum PA amplitude divided by the average PA amplitude in a single modulation cycle. The results of $\Delta PA(D)$, obtained by averaging over 90 modulation cycles, are normalized by the largest value. As shown in Fig. 2.4(b), $\Delta PA(D)$ decays exponentially with increasing thickness D, until it reaches D = 18 mm. The data were fitted with a decay constant of 0.12 mm^{-1}, which describes the speed of depolarization. This

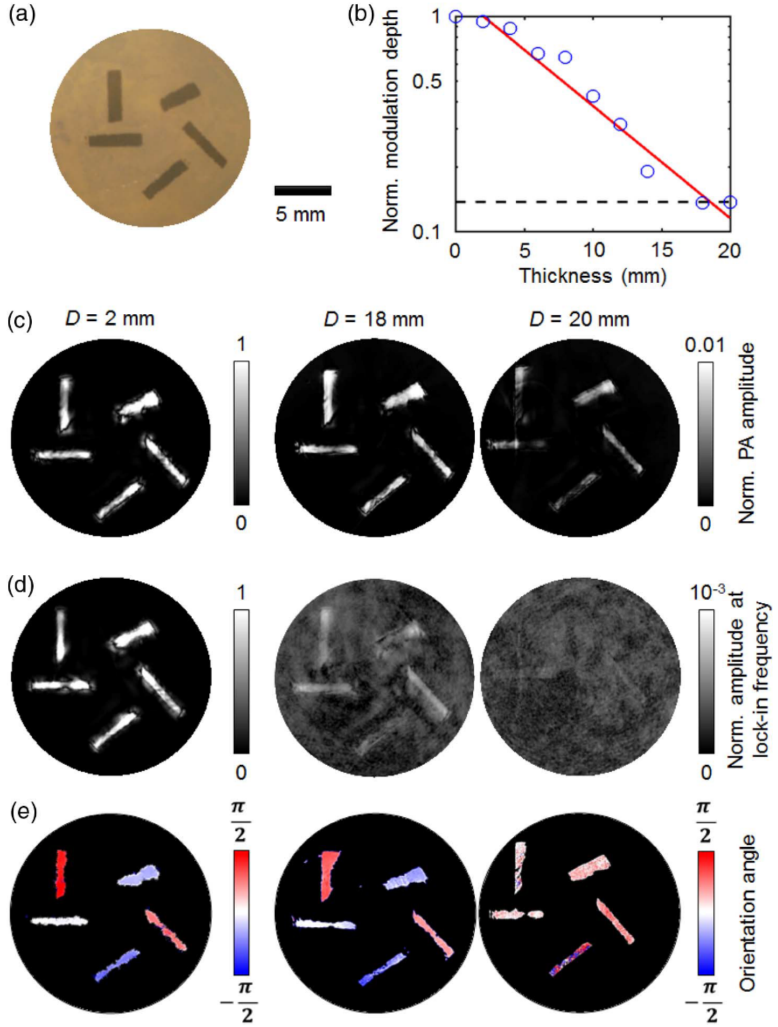

Figure 2.4 DS-PACT of the linear polarizers. (a) Photograph of the sample without any scattering medium. The sample contains five linear polarizers placed at different orientations. (b) Modulation depth of the PA amplitude acquired as a function of thickness D of the scattering medium, up to

20 mm. The red solid line indicates the exponential fit to the measured data. The black dashed line represents the noise level. (c) Conventional PACT images. (d) Amplitude images using DS-PACT. (e) Orientation angle maps of the linear polarizers.

result indicates that DS-PACT can still function at a depth of 18 mm, because the local excitation is still partially polarized. When the thickness reaches D = 20 mm, $\Delta PA(D)$ is dominated by noise, which indicates the depth limit in our current experimental condition. For three representative scattering media with thicknesses of D = 2 mm, 18 mm, and 20 mm, Fig. 2.4(c) shows the reconstructed images using conventional PACT, and all the linear polarizers are visible in all three images. We also reconstructed the images using DS-PACT. The amplitude image and the orientation angle map are shown in Figs. 2.4(d) and (e). As we can see from the figure, even below an 18 mm thick scattering medium, the linear polarizers are still visible, and the orientations of their optic axes can still be detected. However, when D = 20 mm, the amplitude of the lock-in term becomes too weak, so that the linear polarizers disappear from the DSPACT image [Fig. 2.4(d)], and the orientation angle map is no longer correct [Fig. 2.4(e)]. Therefore, we conclude that under our current experimental conditions DS-PACT can image linear polarizers at 18 mm deep, which is approximately equal to 4.5 transport mean free paths.

Ex Vivo Experiment

To show that DS-PACT is suitable for biological applications, we also formed images of biological tissue in scattering media. In experiments, we imaged two pieces of *ex vivo* bovine tendon [27] [Fig. 2.5(a)], a typical dichroic tissue, at various depths below the scattering medium. Bovine tendon has a high concentration of collagen, which exhibits optical dichroism and absorbs strongly at 532 nm. Figure 2.5(b) shows the normalized modulation depth $\Delta PA(D)$ for the bovine tendon as a function of D, with a result similar to that in Fig. 2.4(b). $\Delta PA(D)$ decays exponentially until it reaches $D = 13$ mm, and finally encounters the noise level at $D = 15$ mm. The decay constant of the best-fitting line was 0.1 mm^{-1}. For three representative scattering media with thicknesses of $D = 2$ mm, 13 mm, and 15 mm, Fig. 2.5(c) shows the reconstructed images using conventional PACT, and both pieces of bovine tendon are visible in all three images. We also reconstructed the images using DS-PACT. The amplitude images and the orientation angle maps are shown in Fig. 2.5(d) and (e), respectively. As we can see from the figure, the bovine tendons are still visible when the scattering medium has a thickness of $D = 13$ mm, and the orientation of their optic axes can still be detected. However, when $D = 15$ mm, the amplitude of the lock-in term becomes too weak, so

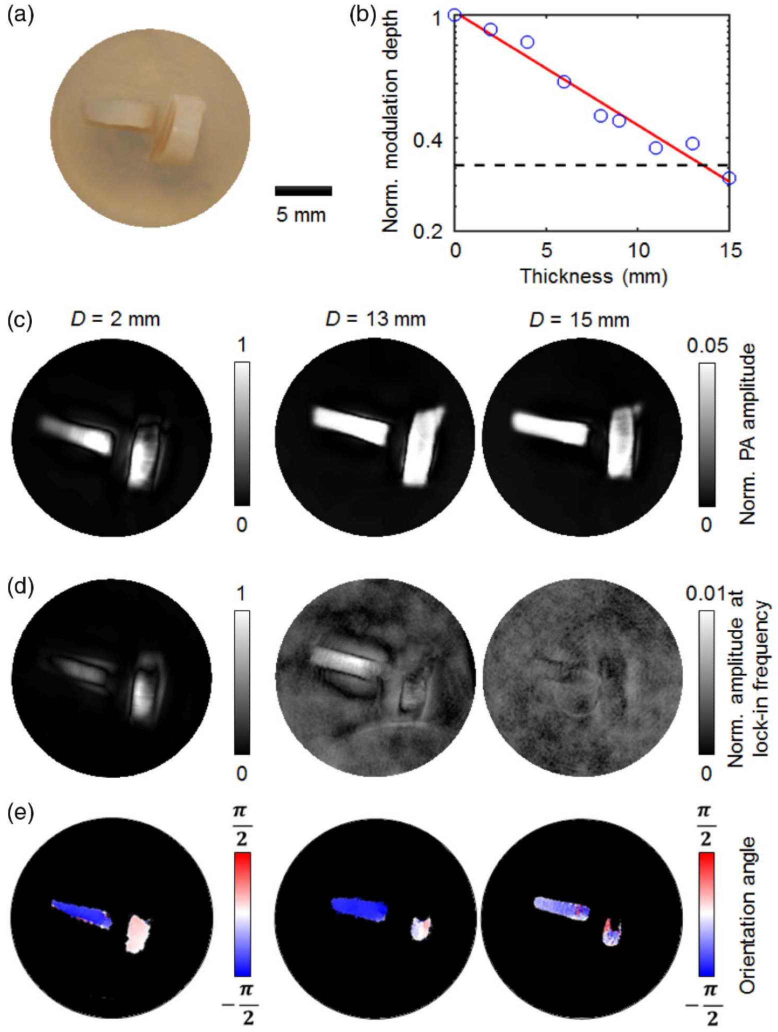

Figure 2.5 DS-PACT of bovine tendons. (a) Photograph of the sample without any scattering medium. The sample contains two pieces of bovine tendon, which are placed perpendicular to each other. (b) Modulation depth of the PA amplitude acquired with increasing thickness D of the scattering medium, up to 15 mm. The red solid line indicates the exponential fit to the measured data. The black dashed line represents the noise level. (c) Conventional PACT images. (d) Amplitude images using DSPACT. (e) Orientation angle maps of the two pieces of bovine tendon.

that the two pieces of bovine tendon disappear from the DS-PACT image [Fig. 2.5(d)], and the orientation angle map is no longer correct [Fig. 2.5(e)]. Thus, the deepest penetration of DS-PACT demonstrated using the bovine tendon in our experiments was 13 mm, approximately equal to 3.25 transport mean free paths.

2.4 Discussion

In conclusion, we have developed a new approach to image the dichroism of biological tissues and detect their orientations at a depth much beyond the ballistic regime. This approach introduces new possibilities for biomedical applications of PACT. For example, the disruption of cell polarity is a hallmark of carcinomas [29], and conventional optical polarization imaging can image this phenomenon [30] with only shallow penetration. DS-PACT may hold a potential for quantifying carcinoma invasion. Further development of our imaging modality could include the use of near-infrared light illumination and a long acquisition sequence to extend the penetration depth. Also, the development of this technique towards clinical application in the next step should focus on integrating this method with a PA endoscope.

Chapter 3: Transvaginal acoustic-resolution photoacoustic endoscope for functional imaging

This chapter introduces the development of photoacoustic endoscopy for human cervical imaging. The side-scanning photoacoustic probe is 20 mm in diameter and has an ~10 Hz B-scan rate. Here, we describe the mechanical design and present *in vivo* experimental results suggesting its potential for clinical applications.

3.1 Background

Nowadays, the imaging instruments used to diagnose urogenital diseases, such as endometrial cancer, cervical cancer, and prostate cancer, are inadequate [31]. More effective tools are desired to achieve accurate medical assessments. As an emerging imaging modality [13], photoacoustic endoscopy (PAE) use a photoacoustic (PA) tomography system in a miniaturized probe to enable high-resolution imaging of internal organs with optical absorption contrast. PAE is good at visualizing blood vasculature as well as dye-labeled lymph vessels, providing structural and functional information *in vivo* [32-34]. The imaging capability of PAE can be extended to acquiring other physiological information, for example, glucose metabolism and micro-hemodynamics, as demonstrated by tabletop systems [35,36]. PAE can also reveal angiogenesis and abnormal metabolic rates, both of which are common harbingers of neoplasms. Therefore, the information from PAE can potentially benefit diagnosis and treatment monitoring for many diseases.

Many PAE systems have been demonstrated for intravascular [37], urogenital [38], and gastrointestinal [33] imaging, but only two imaging probes have reported *in vivo* imaging with a fully encapsulated probe, a feasible size for endoscopy, and a fast scanning speed [33,34]. Other reported probes have not shown *in vivo* images. Moreover, the flexible imaging probes reported in Refs. [33,34] are not suitable for transvaginal imaging, which requires a rigid structure. Furthermore, the small diameter of endoscopic probes (< 4 mm) is unnecessary in this environment, considering the extensive use of large-diameter ultrasound probes for many urogenital disease diagnoses [39]. Here, we implement a new endoscopic probe with improved sensitivity and a higher frame rate. In our design, the ultrasonic transducer faces towards the tissue surface so that we successfully avoid the loss of acoustic energy due to reflection [33]. The high imaging speed is attributed to the miniaturized servo motor which drives the mechanical scanning, covering ± 15°.

3.2 Methods

Figure 3.1(a) shows a schematic of our imaging system. The light source is a dye laser (Cobra, Sirah Lasertechnik) that tunes the wavelength between 562 nm and 578 nm. The beam passes through an iris which helps control the light power. In the optical setup, a beamsplitter reflects 10% of the light energy to a photodiode that monitors the power fluctuations pulse by pulse. The rest of the energy is coupled into a multimode optical fiber. We wrote a custom LabVIEW program to control the whole system through a computer and a control box. To stabilize the mechanical scanning, we employ a proportional-integral-derivative (PID) microcontroller (Arduino Mega 2560) in the control box, based on the feedback from a rotary encoder (Fig. 3.1b). To record PA signals, we utilize a high-speed digitizer (ATS9350, Alazar Technologies). A multifunction data acquisition card (PCI-6221, National Instruments) in the control box controls the peripheral system and records the output of the photodiode. We record 423 A-lines per B-scan, which yields an angular step size of 0.072°.

We fabricated the probe housing from a medical-grade stainless steel tube (MicroGroup) with an outer diameter of 20 mm and a length of ~20 cm. The handle of the probe (Fig. 3.1b and c) contains a servo motor (G330, GSI group) for scanning, a rotary encoder (HEDS-9100, Avago Technologies) for stabilizing the scanning in operation, and a signal amplifier. The insertion tube, which is full of distilled water for PA imaging, is sealed to protect the electronics in the handle. In the insertion tube, a custom ring ultrasonic transducer (Capistrano Labs) facing towards the tissue can detect PA signals excited by the light delivered through the hole of the ring transducer. We use an optically and acoustically transparent polyethylene terephthalate membrane (103-0227, Advanced Polymers) as the imaging window. The diameter of the unfocused laser beam on the tissue surface underneath the window is ~3 mm, so the spatial resolution of the PA imaging is determined by the ultrasonic transducer. To image cervical vasculature, we set the working distance at ~2 mm from the probe surface. For this target, light can penetrate only ~3 mm in general, because a considerable number of blood vessels occupy the superficial layers in a cervix and absorb most of energy in this region.

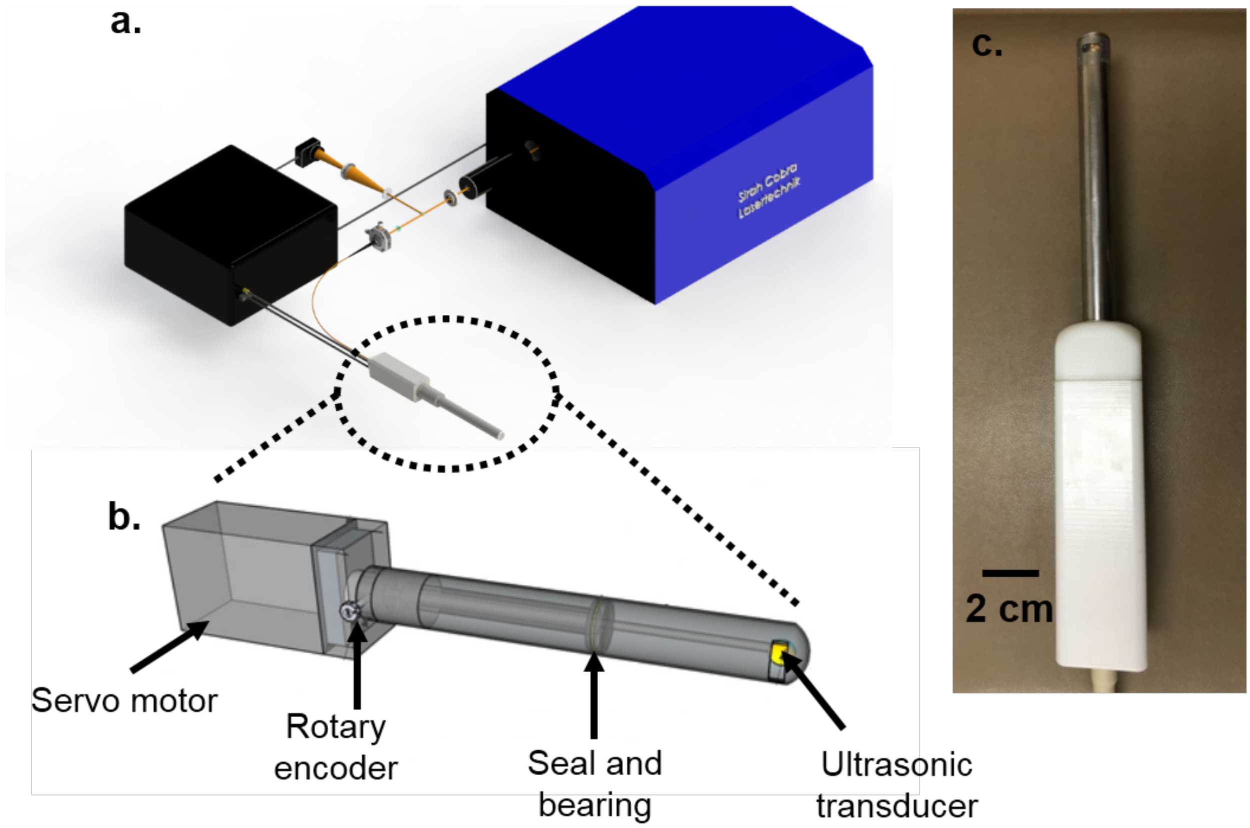

Figure 3.1 Experimental setup. (a) Schematic of the PAE system. (b) Schematic of the PAE probe. (c) Photograph of the PAE probe.

3.3 Results

Phantom Experiment

We tested the imaging performance of our acoustic-resolution (AR) PA endoscope. Benefitting from the capacity of the servo motor, our endoscope's scanning speed could reach 100 Hz. In experiments to be presented later, however, we recorded images at a B-scan frame rate of 10 Hz, which is enough to monitor the dynamics of hemoglobin [40] and oxygen saturation [14], because of the limited pulse repetition rate of our laser. For the resolution measurement, we utilized a resolution chart provided by National Institute of Standards and Technology, as a target (Fig. 3.2a).

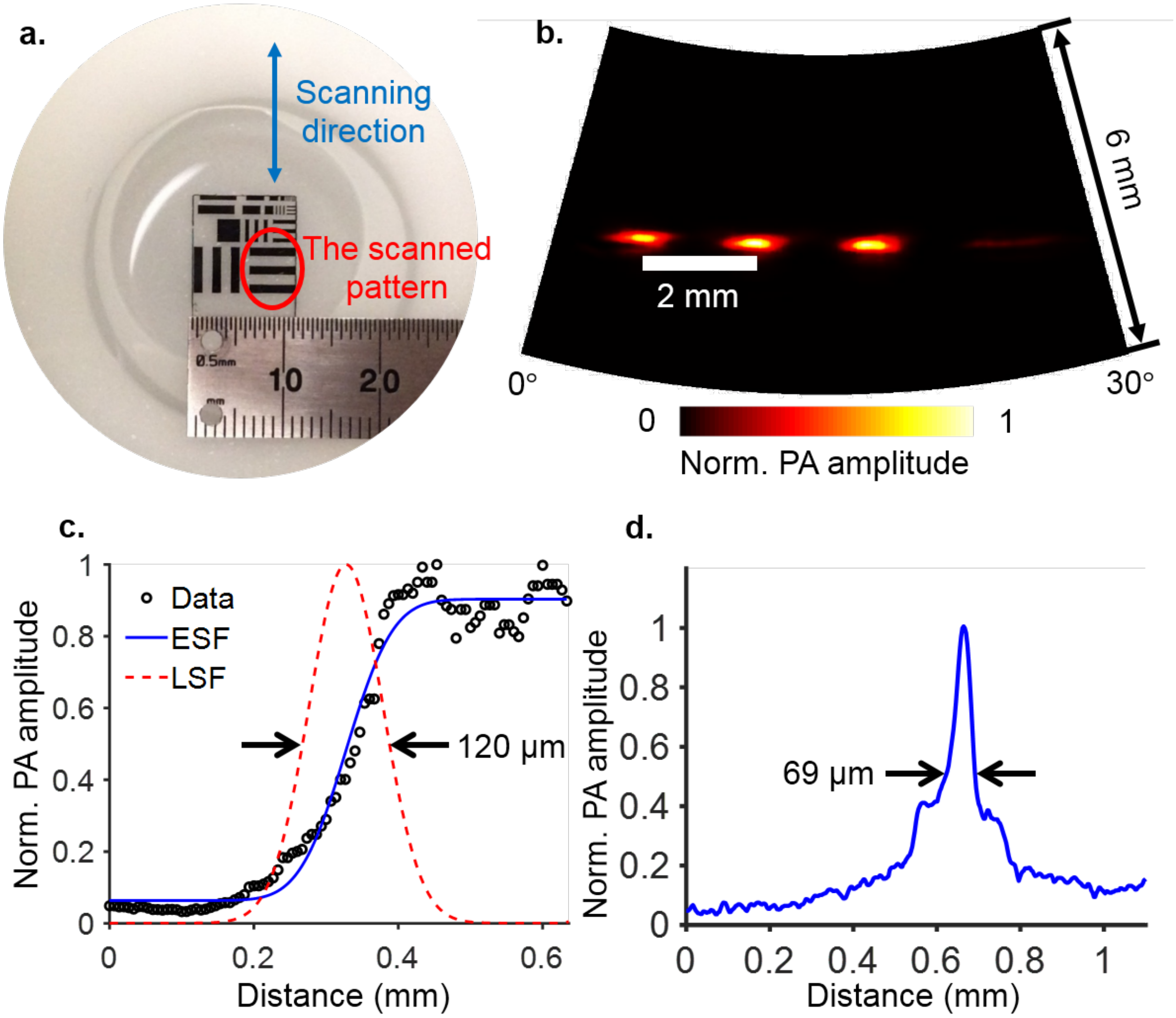

Figure 3.2 AR probe performance. (a) Photography of resolution chart. (b) PA B-scan image of the resolution chart in the red circle highlighted in (a). (c) Lateral resolution test on the resolution

chart. ESF, edge spread function; LSF, line spread function. (d) Hilbert-transformed PA A-line signal for the resolution chart.

The imaged black stripes, 1 mm wide and 1 mm apart, have sharp edges and thicknesses on the scale of nanometers. The corresponding PA B-scan image is shown in Fig. 3.2b. The lateral resolution of the AR probe was quantified by analyzing the line spread function with respect to the edge of a black stripe. The full width at half maximum (FWHM) of the line spread function is 120 μm (Fig. 3.2c). In comparison, Fig. 3.2d shows the Hilbert transformed PA A-line signal, whose FWHM is 69 μm.

Human Experiment

This protocol was approved by the Institutional Review Board of Washington University in St. Louis (IRB # 201505107). The purpose of this study is to apply novel PAE for cervical imaging using recently developed photoacoustic imaging probes. PAE can obtain anatomic and functional information about the cervical microenvironment that will permit early detection of preterm birth.

The endoscopic system provides anatomic information about the human cervix, covering an approximately 7 mm wide, 3 mm deep region (Fig. 3.3a). We reconstructed the PA image from data acquired at a 562-nm laser wavelength in which the photoacoustic signal is proportional to the total hemoglobin concentration. Both the *ex vivo* (Fig. 3.3a, left) and *in vivo* (Fig. 3.3a, right) images show blood vessel distribution. In the images, it seems that the hysterectomy cervical sample has more blood in the entire field of view. This phenomenon may be attributed to bleeding in the hysterectomy and angiogenesis in the development of cervical cancer. Beyond anatomic information, the endoscope also provides functional information, such as the saturation of oxygen (sO2). To reconstruct the sO2 distribution over the scanned area (Fig. 3.3b), we spectrally analyzed dual-wavelength PA images. The *ex vivo* sample shows a relative hypoxic state, because there was no blood flow for an hour after the hysterectomy (Fig. 3.3c). The experiment clearly illustrates that our endoscope can image blood distribution and sO2 in tissues.

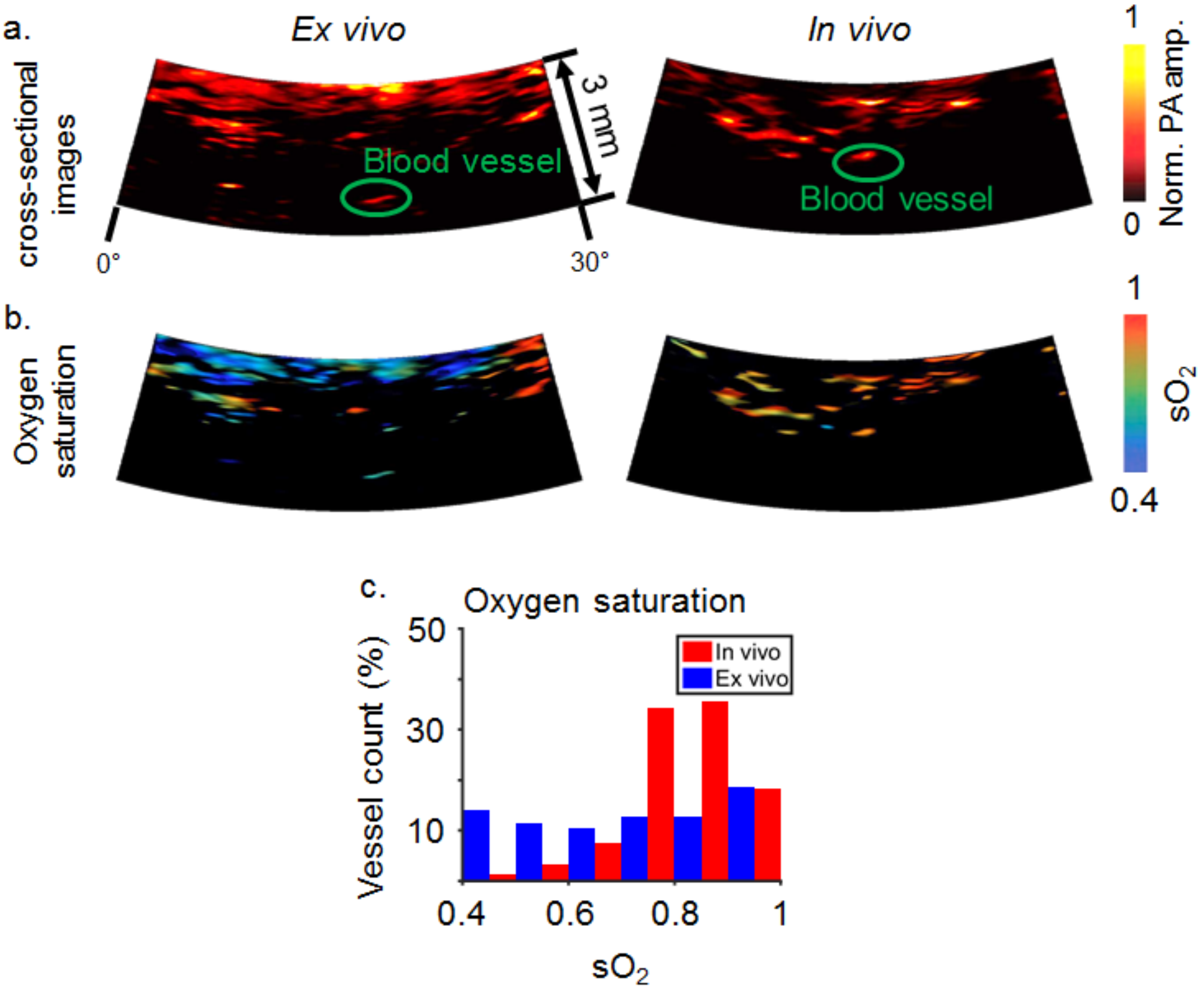

Figure 3.3 (a) PA and (b) oxygen saturation images from a hysterectomy sample *ex vivo* (left) and a human cervix *in vivo* (right). (c) Comparison of oxygen saturation levels in the hysterectomy sample (blue) and human cervix (red).

3.4 Discussion

In this study, we designed and implemented a dual-wavelength PAE for human transvaginal imaging and demonstrated its endoscopic capability through *ex vivo* and *in vivo* experiments. The endoscopic probe enabled functional PA imaging with a B-scan frame rate of 10 Hz, which is fast enough to monitor the dynamics of hemoglobin and oxygen saturation. In comparison with our previous stepper-motor-based endoscope [41], the current design positions the transducer directly facing the tissue, which improves the PA detection sensitivity, and the servo motor is mounted in the probe handle. This arrangement better separates the scanning components from the water that fills the probe and increases the reliability and longevity of the probe. By relocating the signal amplifier to the handle, the signal-to-noise ratio of the imaging system is further improved. Although the endoscope's design probably needs to be modified for specific applications, the general concept and scanning mechanism presented here will be useful for various other applications, for example a hand-held PA probe [42].

The limited imaging depth of this endoscope in the *in vivo* experiment, ~ 3 mm, is the main technical challenge to clinical applications, because many capillaries are distributed near visceral surfaces and they dissipate most of the energy in the light. For this prototype, the limited focal zone of the transducer yields poor spatial resolution. Applying the concept of photoacoustic computed tomography [21,43] could improve the transverse resolution over the entire field of view. Our next goal is to apply this endoscope to monitor the change of oxygen saturation in tissue throughout pregnancy.

Chapter 4: In vivo characterization of connective tissue remodeling using infrared photoacoustic spectra

In chapter 4, I elaborate a method to quantify tissue hydration using photoacoustic endoscopy. Premature cervical remodeling is a critical precursor of spontaneous preterm birth, and the remodeling process is characterized by an increase in tissue hydration. Nevertheless, current clinical measurements of cervical remodeling are subjective and detect only late events, such as cervical effacement and dilation. Here, we present a photoacoustic endoscope that can quantify tissue hydration by measuring near-infrared cervical spectra. We quantify the water contents of tissue-mimicking hydrogel phantoms as an analog of cervical connective tissue. Applying this method to pregnant women *in vivo*, we observe an increase in the water content of the cervix throughout pregnancy. The application of this technique in maternal healthcare may advance our understanding of cervical remodeling and provide a sensitive method for predicting preterm birth.

4.1 Background

The cervix is a remarkable structure with diametrically opposite functions: it maintains pregnancy by remaining closed and then, in a process called remodeling, softens and dilates to allow delivery of the fetus in labor [7]. Premature cervical remodeling is a critical indicator of impending spontaneous preterm birth. Preterm birth can occur with a remodeled cervix even in the absence of uterine contractions, but uterine contractions do not lead to delivery if the cervix is firm [44-

46]. Nevertheless, current clinical measurements of cervical remodeling are largely obtained by digital examinations, which are subjective and detect only late events, such as cervical effacement and dilation.

The cervix remodels progressively via incompletely understood mechanisms, such as degradation of extracellular matrix proteins and inflammation [47,48]. These physiological changes are associated with increased tissue hydration [49,50]. Therefore, a method that can accurately measure cervical hydration during pregnancy has the potential to facilitate our understanding of cervical remodeling and permit more accurate prediction of preterm birth.

Near-infrared spectroscopy is routinely used in industrial applications to quantify the water content in various products, because this method is nondestructive and does not require sample preparation [51,52]. As an embodiment of near-infrared spectroscopy, spectroscopic photoacoustic tomography has been demonstrated in the quantification of various biochemical constituents [53-56]. However, the previous applications used tabletop systems, which precluded *in vivo* use in the gastrointestinal tract and urogenital tract. Photoacoustic endoscopy (PAE) incorporates an acoustic detector, optical components, and electronic components in a millimeter-diameter-scale probe to image tissue that is inaccessible by tabletop systems [32-34,41,57,58].

For the quantification of the water content of the cervix in a pregnant woman, the combination of PAE and near-infrared spectroscopy provides an optimal solution. However, the task is nontrivial, because PAE needs an acoustic coupling medium, which generally contains water as well. The photoacoustic signals emitted by the acoustic coupling medium are not easily separable from the signals emitted by the tissue in the near-infrared wavelength range. This challenge so far has precluded the use of near-infrared spectroscopic PAE for the quantification of water content.

Here, we present a near-infrared spectroscopic PAE system that transmits acoustic waves from the tissue to the acoustic detector through an N-BK7 pentaprism. We analyze the measured photoacoustic near-infrared (PANIR) spectra by linear regression. We demonstrate that this method successfully quantifies the water contents of tissue-mimicking phantoms made of gelatin hydrogel. Applying this method to the cervixes of pregnant women, we observe their physiological water contents and a progressive increase throughout gestation.

4.2 Methods

We developed the PANIR system shown in Fig. 4.1(a). The system is controlled by a custom-designed program written in LabVIEW (National Instruments). A frequency-tripled Nd:YAG laser (Quantel, Q-smart 450), operating at 355-nm wavelength with a 20-Hz pulse repetition rate, pumps an optical parametric oscillator (GWU-Lasertechnik, basiScan). A stepper motor moves the optical parametric oscillator so that the idler light can be scanned from 1000 to 2000 nm. After passing through the oscillator, the remaining energy of the pump light is absorbed by a longpass filter. The idler light is selected by a dichroic mirror and then coupled into a multimode fiber, which guides the light to the PANIR probe [Fig. 4.1(b)]. An iris between the dichroic mirror and the fiber coupler controls the delivered optical energy, keeping the optical fluence (mJ/cm2) on the tissue surface below the American National Standards Institute safe exposure limit [23].

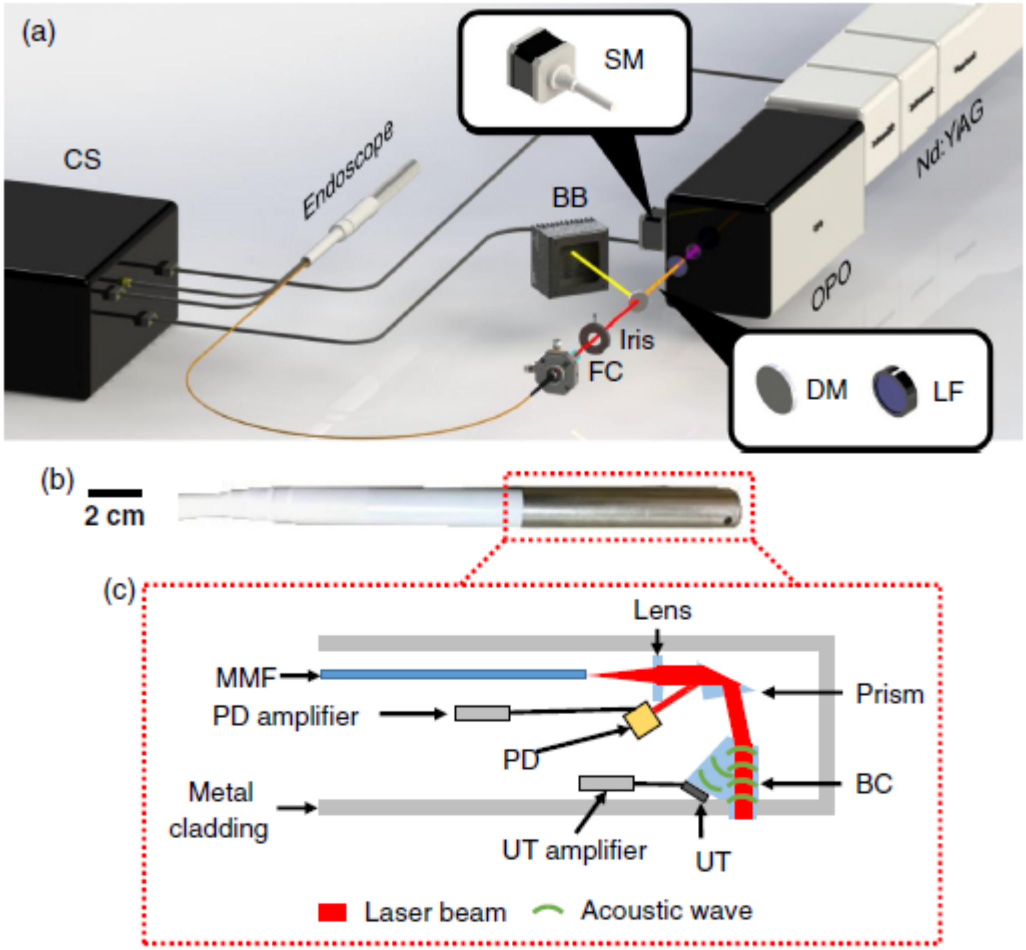

Figure 4.1 PANIR system. (a) Setup of the PANIR system. BB, beam block; CS, control system; DM, dichroic mirror; FC, fiber coupler; LF, longpass filter; Nd:YAG, Nd:YAG laser with a frequency tripling module; OPO, optical parametric oscillator; SM, stepper motor. (b) Photograph of a PANIR probe. (c) Schematic of the components in the probe. BC, beam combiner; MMF, multimode fiber; PD, calibrated photodiode; UT, ultrasonic transducer.

The internal structure of the PANIR probe, which is 30 cm in the length and 2 cm in the diameter, is shown in Fig. 4.1(c). The idler light from the multimode fiber is projected onto the tissue surface by a plano-convex lens and a prism and is absorbed by the tissue below the optical-acoustic beam combiner—a custom-designed pentaprism. The backward photoacoustic wave propagates through the beam combiner toward an ultrasonic transducer (2.25-MHz central frequency). The configuration of all these optical and acoustic elements reduces the amount of light absorbed by the ultrasonic transducer to a negligible level. While the idler light is sweeping over the entire spectral range, the detected photoacoustic signal is always overwhelmed by noise when only air is underneath the beam combiner. The InGaAs photodiode (FD10D, Thorlabs) in the probe continually measures the energy of the idler light to correct for its energy fluctuations in subsequent data processing. Furthermore, every day, we calibrate the PANIR system with distill water to correct for instrument drift.

We validated the PANIR system by measuring the PANIR spectrum of distilled water at 37.5°C. Fig. 4.2(a) shows the water spectra measured on three dates, and Fig. 4.2(b) shows the respective PA signals measured at a representative wavelength. We did not observe significant instrument drift as the measured spectra were stable.

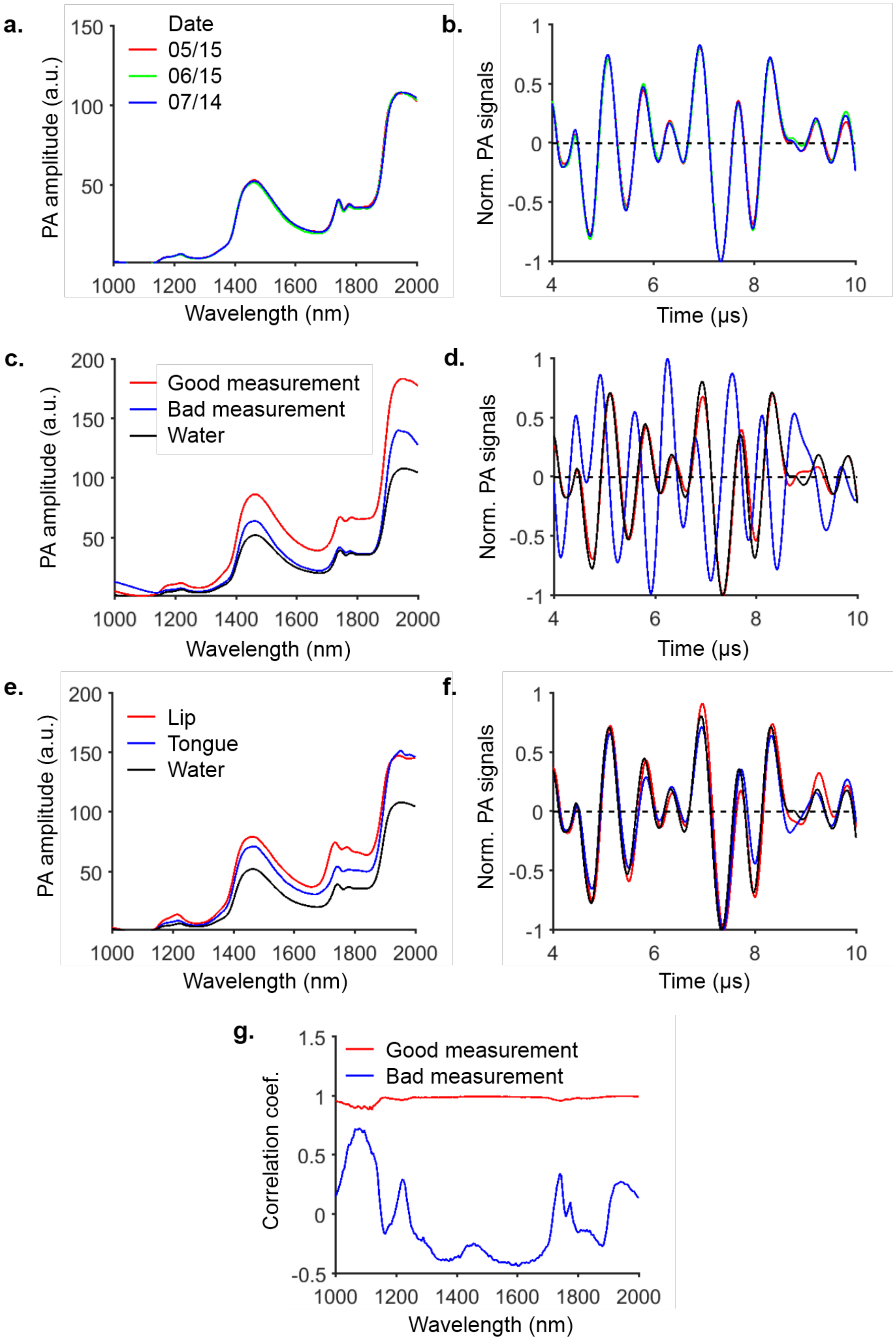
a.
PA amplitude (a.u.)
150
100
50
Date
05/15
06/15
07/14
1000 1200 1400 1600 1800 2000
Wavelength (nm)
b.
Norm. PA signals
1
0.5
0
-0.5
-1
4 6 8 10
Time (μs)
c.
PA amplitude (a.u.)
200
150
100
50
Good measurement
Bad measurement
Water
1000 1200 1400 1600 1800 2000
Wavelength (nm)
d.
Norm. PA signals
1
0.5
0
-0.5
-1
4 6 8 10
Time (μs)
e.
PA amplitude (a.u.)
200
150
100
50
Lip
Tongue
Water
1000 1200 1400 1600 1800 2000
Wavelength (nm)
f.
Norm. PA signals
1
0.5
0
-0.5
-1
4 6 8 10
Time (μs)
g.
Correlation coef.
1.5
1
0.5
0
-0.5
Good measurement
Bad measurement
1000 1200 1400 1600 1800 2000
Wavelength (nm)

Figure 4.2. Assessment of data quality. (a, b) Longitudinal stability of PANIR measurements. We measured distilled water on three dates. The spectra (a) and the photoacoustic signals (b) demonstrate the longitudinal stability of our measurements. (c, d) Sensitivity of PANIR measurements to the boundary condition. We measured human skin in good contact (red) and in bad contact (blue) with the probe window. The boundary condition imposed by the bad contact distorts the spectrum (c) and the photoacoustic signal (d). As a result, the data quality is degraded. (e, f) Sensitivity of PANIR measurements to the types of tissue. The human lip and tongue have different spectra, however, their photoacoustic signals still strongly correlate to the photoacoustic signal from the distilled water (f). (g) Spectra of the Pearson correlation coefficient. By quantifying the similarity in terms of the Pearson correlation coefficient, we can screen the measurements for data analysis.

The predominant factor that affects the PANIR spectral shape is the contact between the probe window and the tissue. A good contact requires the entire window to be directly contacted by the tissue. Any air bubble or liquid in between is likely to distort the detected acoustic wave [Fig. 4.2(d)] and the measured spectrum [Fig. 4.2(c)]. In contrast, although human tissue has microstructures that are obviously much more complicated and heterogeneous than distilled water, and their PANIR spectra are totally different [Fig. 4.2(c)], their PA signals actually share a very similar waveform at the same wavelength when the tissue is in good contact with the probe window [Fig. 4.2(d)]. This similarity reveals three facts in the PANIR measurement. First, the waveform of the excited acoustic wave strongly relates to the spatial profile of the incident laser pulse. Second, the change of the spatial profile between each laser pulse at a given wavelength is too small to significantly distort the waveform. Third, the PA signals emitted by water and by various tissues at a given wavelength show a remarkable similarity, because their acoustic impedances, that is, the imposed boundary condition on the probe window, are approximately equal [59], as demonstrated in Fig. 4.2(c) and (f). Using the human lip and tongue as examples, although their spectra are different [Fig. 4.2(c)], the waveforms detected from them are still similar [Fig. 4.2(f)]. These results suggest that an algorithm quantifying the similarity of waveforms can help to evaluate the data quality.

We calculated the Pearson correlation coefficient [60] between the detected waveform and the reference waveform measured from distilled water at each wavelength. Fig. 4.2(g) shows an example, the correlation spectra calculated for the measurements shown in Fig. 4.2(c) and (d). When the operator positions the PANIR probe in good contact, the correlation spectrum is like a horizontal line close to 1 over the entire wavelength range. Bad contact, on the other hand, results in a correlation spectrum wandering between -1 and 1 over this range.

Participants in our preclinical study were recruited from the patient population attending the Obstetrics and Gynecology Clinic and the Women's Health Center in the Barnes-Jewish Hospital Center for Outpatient Health. Eligibility requirements included an age of 18 or older, the capability of informed consent, and a gestational age of <16 weeks. Exclusions included potential participants who were non-English speaking, unwilling to participate, carrying a twin pregnancy, or showing evidence of major fetal anomalies.

Prior to measuring the cervix, the operator placed a speculum in the vagina, exposing the cervix for PANIR measurements. The PANIR spectrum has a spectral resolution of 5 nm and a scan of one spectrum takes 10s. All experimental procedures were carried out in accordance with the protocols approved by the Institutional Review Board of Washington University in St. Louis. All participants signed informed consents before inclusion in the study.

4.3 Results

Phantom Experiment

We first quantified the water content in phantoms made of hydrogel because of its similarity to connective tissues [61-63]. In phantom preparation, a beaker filled with a mixture of gelatin and distilled water was placed on a hot plate and heated to 90°C. A stir bar stirred the mixture at a constant speed. After the gelatin powder was completely dissolved in the mixture, we let the mixture solidify in a Petri dish at room temperature (20°C). When we measured the PANIR spectrum of the phantom, it was kept at 37.5°C to mimic the temperature of the human cervix, and its weight was measured every hour to track the change of water content due to evaporation. Figure 4.3(a) shows typical phantoms' PANIR spectra, which move upward as the water content decreases.

To quantify the water content, we fitted a single-wavelength linear regression model based on the empirical calibration because the intercorrelation effect of multiwavelength models led to strong instability [51]. To minimize the correlation between our measurements and any variation in the environment, we collected PANIR spectra by random sample selection for both the calibration set and the validation set. The calibration set and the validation set each included 350 PANIR spectra, measured from phantoms whose compositions covered the entire range of water contents in soft human tissues (70% to 100%) [64]. We tested our method at two wavelengths, 1460 nm, corresponding to the first overtone of O─H stretching, and 1940 nm, corresponding to the second overtone of O─H bending [65]. Figures 4.3(b) and 2(c) show the results and confirm that the measurements of water content agree with the preset values. As the water content in the hydrogel decreased, the standard deviation of our measurements increased, because the gel network became more heterogeneous [66], causing the local water content to fluctuate. At either wavelength, the model provided high and similar prediction accuracies.

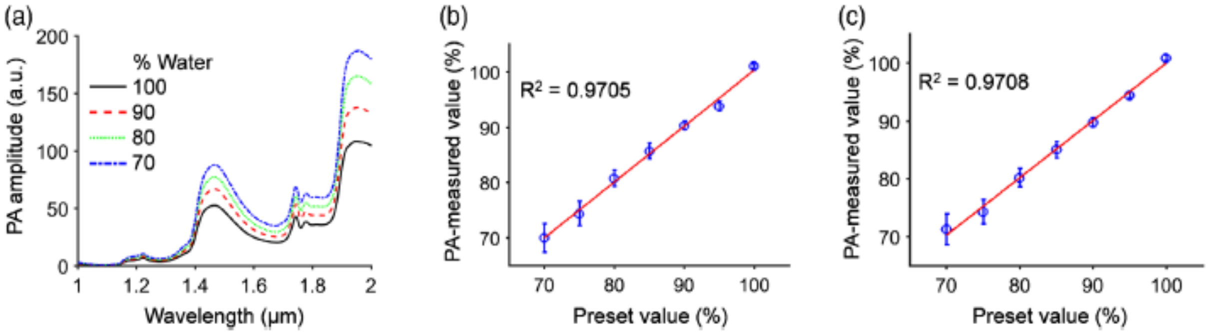

Figure 4.3 PANIR spectra quantify the hydration of hydrogel. (a) PANIR spectra measured from hydrogel phantoms made of water and gelatin with different fractions. (b) and (c) Water contents measured at (b) 1460 nm and (c) 1940 nm versus the preset values.

Simulation of Scattering Effect

For human cervical tissue, we must consider the effect of scattering, which distorts the PANIR spectrum [67]. To understand this influence, we compared our measurements with the results from a Monte Carlo simulation [68] that used the optical properties of human tissue [69]. Figure 4.4(a) shows the distortion of the water spectrum by scattering, comparable with the degree found in human skin. In the wavelength range of 1000 to 1300 nm, where the absorption coefficient ($\mu_a \leq 1$ cm^{-1}) was smaller than the reduced scattering coefficient ($\mu_s' \approx 12$ cm^{-1}), the PANIR spectrum was raised [Fig. 4.4(a)] because more photons were absorbed by water than transmitted [Fig. 4.4(b)]. However, in the neighborhood of 1460 nm, the absorption coefficient ($\mu_a \approx 28$ cm^{-1}) was so large that the scattering ($\mu_s' \approx 11$ cm^{-1}) caused only a small perturbation in the distribution of fluence [Fig. 4.4(b)]. As a result, the scattering has little influence on the amplitudes in this neighborhood [Fig. 4.4(a)]. Without correcting the PANIR spectrum for scattering, the water content of a scattering medium would be underestimated, but only by ~1% [Fig. 4.4(c)]. This underestimation can be neglected as long as the typical change of water content in a physiological process is much >1%. In addition, the standard deviation of water contents caused by the cross-sectional change of scattering among the tissue samples was about one order smaller than the underestimation.

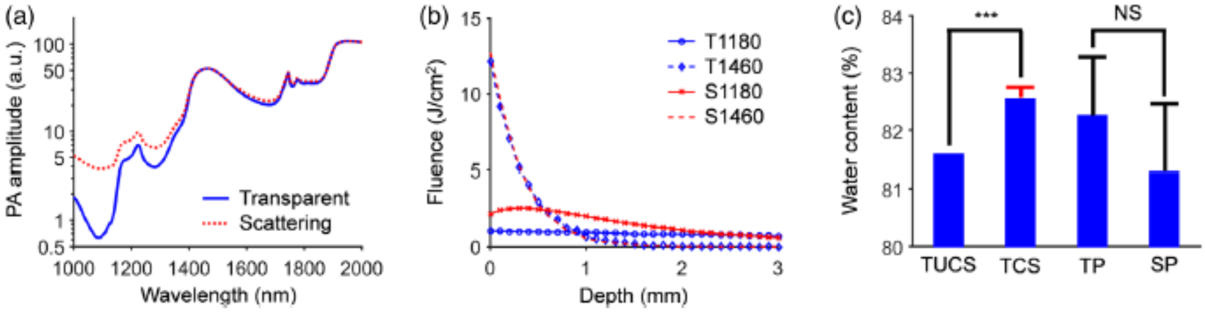

Figure 4.4 Effects of scattering simulated by the Monte Carlo method. (a) Effect of scattering on the spectrum. We measured the PANIR spectrum of distilled water (blue) and calculated its spectrum distorted by scattering (red), comparable with the degree found in human skin. (b) Effect

of scattering on the distributions of fluence in a medium. The absorption at 1460 nm is so strong that the scattering leads to only a small perturbation of the distribution of fluence. S1180, simulated at 1180 nm in the scattering medium; S1460, simulated at 1460 nm in the scattering medium; T1180, simulated at 1180 nm in the transparent medium; T1460, simulated at 1460 nm in the transparent medium. For illustrative purposes, T1460 and S1460 are divided by a factor of two. (c) Quantified water contents for the human tissue and the hydrogel phantoms. The transparent model underestimates the water content of the scattering medium by ∼1%. The red error bar and the black error bar, respectively, show the standard deviations contributed by the cross-sectional change of scattering among the tissue samples (n = 16) [69] and by the heterogeneity of the hydrogel phantoms (n = 10). SP, scattering phantom; TCS, tissue corrected for scattering; TP, transparent phantom; TUCS, tissue uncorrected for scattering. ***, $P < 0.001$. NS, nonsignificant.

Furthermore, we compared the simulation to a phantom experiment in which we made one transparent phantom (hydrogel with 18% gelatin) and one scattering phantom (hydrogel with 1% Intralipid and 17% gelatin). The linear regression model underestimated the water content by ∼1% in the scattering phantom, where the reduced scattering coefficient approximated the values used in our simulation. The underestimations in the phantom experiment and in the simulation were consistent. Meanwhile, the heterogeneous gel network resulted in a larger standard deviation of water contents in the measurement, in comparison with the cross-sectional change of scattering in the simulation. These results suggest that scattering will have a minor effect, and the heterogeneity of human tissue will dominate the variation of measured water contents in application.

Clinical Experiment

We validated this method in serial and cross-sectional human studies (Fig. 4.5), based on the assumption that the hydrogel and the cervical connective tissue were so similar that the regression model derived from one could be applied to the other [61-63]. Figure 4.5(a) shows the PANIR spectra of a pregnant woman at five gestational time points. The PANIR spectra of the cervix showed little change before 20 weeks' gestation and then dropped to a lower level at the end of the second trimester.

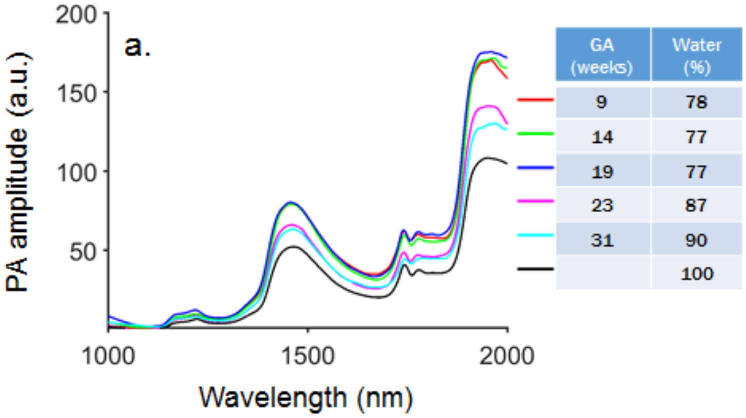

Figure 4.5 PANIR spectra quantify cervical remodeling. (a) PANIR spectra measured from the cervix of a pregnant woman at five gestational time points.

4.4 Discussion

We have developed *in vivo* PANIR endoscopy that measures the cervical PANIR spectra of pregnant women. With this new technique, we observed serial and cross-sectional changes in PANIR spectra and cervical hydration in pregnancy. Moreover, the measured cervical hydration was consistent with empirically measured values [70]. Measurement of PANIR spectra and the cervical hydration levels by our system introduces new possibilities for studying preterm birth. They have the potential to explain how environmental or patient-specific factors increase the risk of preterm birth [71-75].

Further research and development of our technology could include direct analysis of PANIR spectra using comprehensive machine learning models, which might reveal other phenomena latent in the spectra beyond human perception [76,77]. In addition, the reconstructed PANIR spectrum was a mean spectrum from the area under the beam combiner because the photoacoustic signal was detected by a single-element transducer. As a result, the current lateral spatial resolution is ~2.5 mm. Employing a transducer array and photoacoustic computed tomography [17,20] may enable mapping the PANIR spectrum over the same area with a 100 μm spatial resolution. Other optical methods for quantifying cervical remodeling in pregnant women are being developed [78-82]. Comparing all optical methods in a large-scale preclinical study would advance our understanding of cervical remodeling from multiple aspects and maximize the prediction accuracy of premature cervical remodeling and preterm birth.

Chapter 5: Transvaginal fast-scanning optical-resolution photoacoustic endoscopy

Photoacoustic endoscopy offers *in vivo* examination of the visceral tissue using endogenous contrast, but its typical B-scan rate is ∼10 Hz, restricted by the speed of the scanning unit and the laser pulse repetition rate. In this chapter, we present a transvaginal fast-scanning optical-resolution photoacoustic endoscope with a 250-Hz B-scan rate over a 3-mm scanning range. Using this modality, we not only illustrate the morphological differences of vasculatures among the human ectocervix, uterine body, and sublingual mucosa but also shows the longitudinal and cross-sectional differences of cervical vasculatures in pregnant women. This technology is promising for screening the visceral pathological changes associated with angiogenesis.

5.1 Background

Vasculatures enable nutrient transportation, waste disposal, and immune surveillance. Due to the diverse functions of blood vessels, abnormally morphological vascular changes are often associated with the development of various diseases, including tumor growth and metastasis [83,84], inflammatory disorders, and pulmonary hypertension [85], to name just a few. Many models linking vascular morphogenesis to the development of a particular disease have been developed for prognosis, diagnosis, or disease management [86]. To apply these models in clinical assessment, however, a tissue biopsy from the lesion is needed. Because tissue biopsy is invasive and often not clinically feasible [87], technologies that provide *in vivo* noninvasive examination of vascular networks are clinically useful [88], but generally do not have enough resolution and specificity to resolve microcirculation vessels.

Optical-resolution photoacoustic microscopy using endogenous optical absorption contrast enables *in vivo* vascular imaging with a capillary-level spatial resolution, and it has emerged as a major tool for inspecting morphological changes in the vascular network [89]. Photoacoustic endoscopy (PAE), by miniaturizing the tabletop setup of photoacoustic microscopy, can reach organs in body cavities and noninvasively acquire visceral vascular images [32-34]. These endoscopic devices use rotary scanners, which enable a large angular field of view, up to ∼310 degrees, but also constrain the B-scan rate to ∼10 Hz. As a result, motion artifacts due to the natural *in vivo* movement of tissue (breathing movement, peristalsis, etc.) often appear in the endoscopic images. Thus, the development of new PAE systems with higher imaging speeds is a top priority to broaden its clinical application. Microelectromechanical system (MEMS) scanning mirrors have demonstrated their superior scanning speed, high accuracy, and simple system design in various biomedical imaging modalities [90,91]. A water-immersible version with a small footprint has the potential to increase the imaging speed of PAE by an order of magnitude.

Here, we present a fast-scanning optical-resolution PAE (fsOR-PAE) that uses a custom-designed MEMS scanning mirror. The B-scan rate can reach 250 Hz over a 3-mm range, faster than the previous device by a factor of 10 [41]. This imaging speed allowed us to acquire visceral vascular images in humans *in vivo*, with a volumetric imaging speed of 0.75 Hz.

5.2 Methods

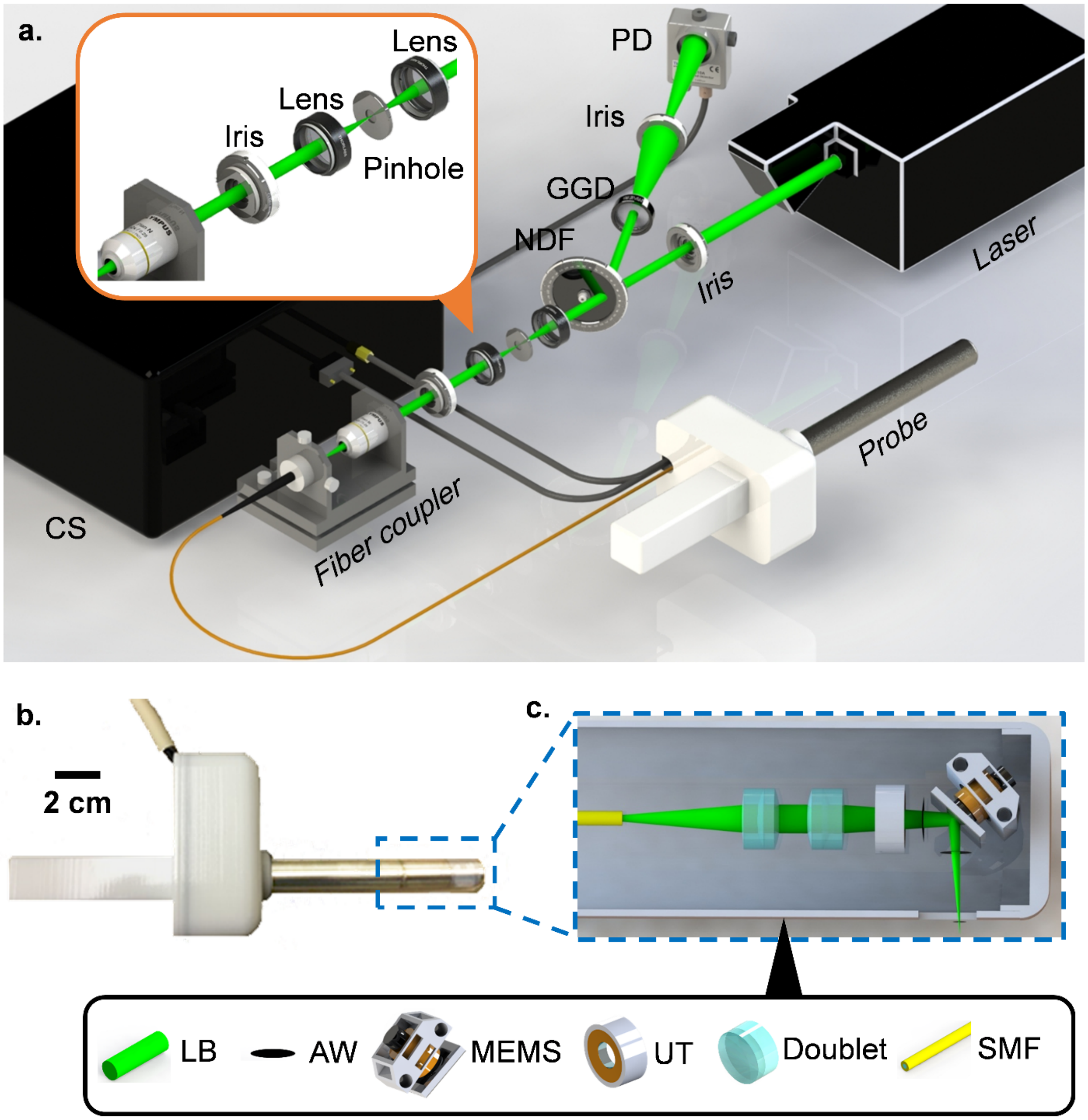

Figure 5.1 Schematic of the fsOR-PAE probe and its peripheral systems. (a) Setup of fsOR-PAE. CS, control system; GGD, ground glass diffuser; NDF, variable neutral density filter; PD, photodetector. (b) Photograph of the fsOR-PAE probe. A linear actuator in the white housing drives the azimuth scanning. (c) Schematic of the acoustic-optical coaxial confocal alignment in

the probe. MEMS drives the scanning parallel to the cylindrical axis. AW, acoustic wave; LB, laser beam; MEMS, microelectromechanical system scanning mirror; SMF, single-mode fiber; UT, ultrasonic transducer.

Figure 5.1 is a schematic of our fsOR-PAE system. The system [Fig. 5.1(a)] is controlled by a custom-designed program written in LabVIEW (National Instruments). A fiber laser (V-Gen, VPFL-G-20) operates at 532-nm wavelength with a 500-kHz pulse repetition rate. We control the laser pulse energy by tuning a variable neutral density filter so that the optical fluence on the tissue surface is ∼17 mJ/cm^2, below the American National Standards Institute safe exposure limit [23]. A photodetector (Thorlabs, PDA36A) detects the light reflected from the neutral density filter, and a voltage comparator connected to the photodetector generates a trigger for each laser pulse to synchronize the whole system. The laser beam is spatially filtered by a 50-μm diameter pinhole (Thorlabs, P50CH) before being coupled into a single-mode optical fiber (Thorlabs, S405-XP). The fiber guides the light to the fsOR-PAE probe with an insertion tube 20 cm in length and 20 mm in diameter [Fig. 5.1(b)].

In the probe, the laser beam from the single-mode fiber is focused by a set of doublets (Thorlabs, AC064-015-A) and then transmitted through the center of a custom-designed focused ultrasonic ring transducer (40-MHz central frequency), achieving an acoustic-optical coaxial confocal alignment [Fig. 5.1(c)]. To optimize the optical and acoustic transmittances through the imaging window, a polymethylpentene membrane (CS Hyde, 33-3F-24) seals the imaging window, preventing leakage when the chamber of the probe is filled with distilled water for ultrasound coupling. A MEMS scanning mirror drives the focal spot scanning parallel to the cylindrical axis of the probe [Fig. 5.2]. It has two hinges (0.75 mm in length, 0.5 mm in width, and 0.2 mm in thickness) supporting a mirror plate (7 mm in length, 5 mm in width, and 1 mm in thickness), which consists of a polished silicon substrate, an aluminum reflective layer (200 nm), and a SiO2 protective overcoat (20 nm). The fast scanning is attributed to the oscillation of the mirror plate: a pair of permanent magnets fixed on the back of the mirror plate oscillate around the hinges in response to a sinusoidal current applied to the static inductor coil (inductance: 1 μH) in the MEMS device. The azimuthal scanning, with a step size of 3 μm, is driven by a linear actuator (Haydon Kerk, 21F4AC-2.5) in the white housing of the probe.

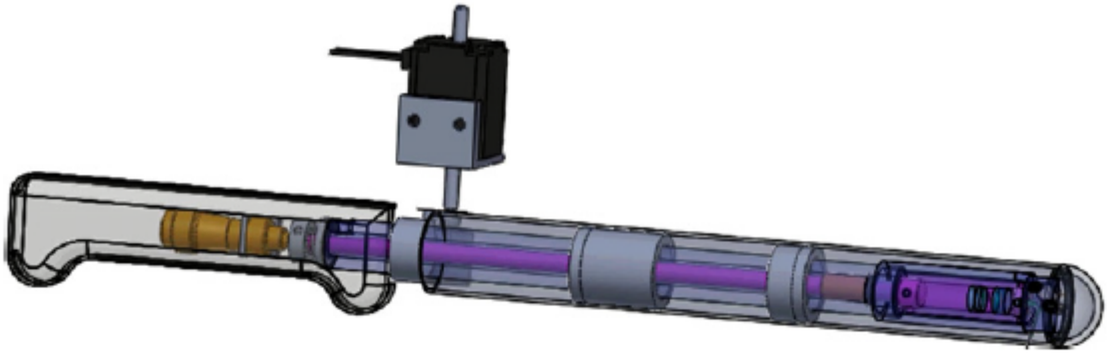

Figure 5.2 Scanning mechanism of the fsOR-PAE probe.

5.3 Results

Phantom Experiment

To test the performance of the fsOR-PAE system, we imaged tissue-mimicking phantoms. The lateral resolution of fsOR-PAE was quantified by imaging the edge of a sharp blade. From the edge spread function, the line spread function was computed and found to have a full width at half maximum of 3.1 µm, which represents the lateral resolution [Fig. 5.3(a)]. The axial resolution was estimated to be 46.5 µm, based on the photoacoustic signal detected from a tungsten wire (diameter: 14 µm) [Fig. 5.3(b)]. A metal grid (127-µm pitch and 37-µm bar width) [Fig. 5.3(c)] was imaged [Fig. 5.3(d)], and the average signal-to-noise ratio (SNR) was 33.2 dB. Figure 5.3(e) is a B-scan image in the plane highlighted by the dashed line in Fig. 5.3(d). Because the angular scanning of fsOR-PAE maps the detected photoacoustic signal in polar coordinates, we transform the data to Cartesian coordinates in image reconstruction [91]. These results suggest that the fsOR-PAE system is capable of imaging structures on the micrometer scale.

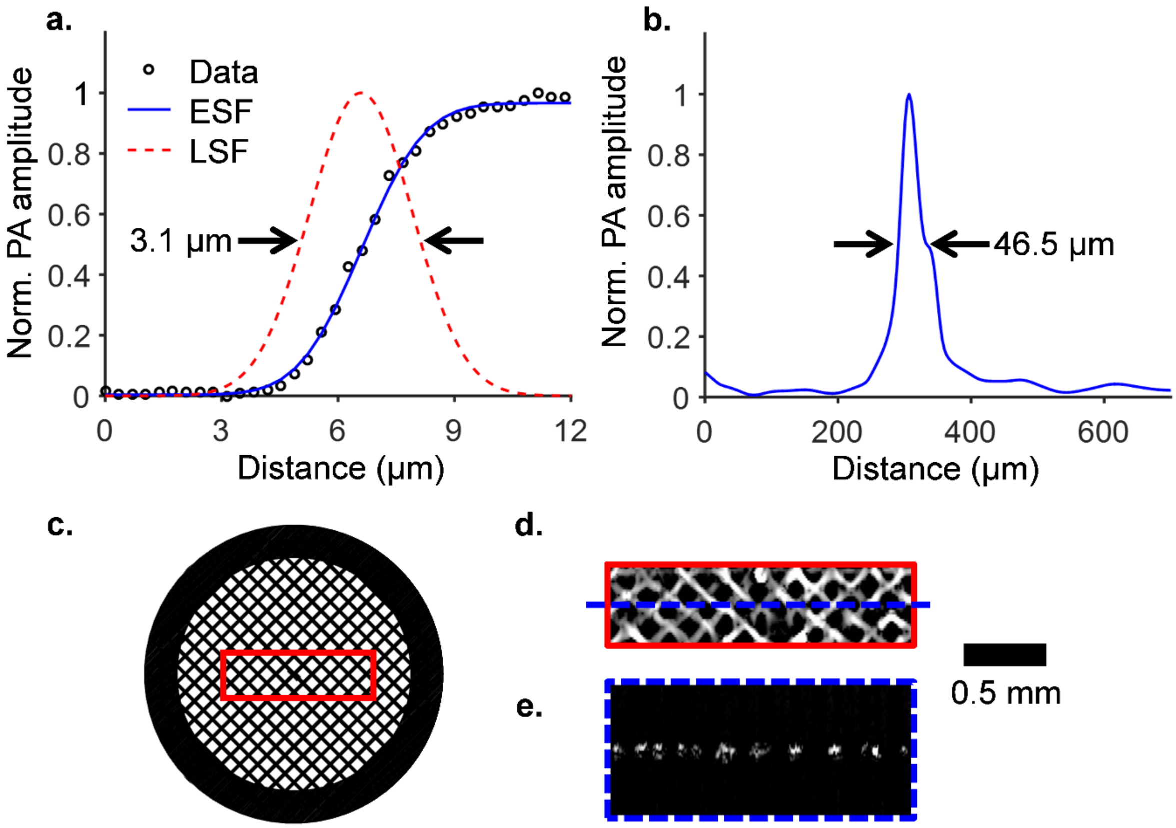

Figure 5.3 Characterization of the fsOR-PAE probe. (a) Lateral resolution test on a sharp edge. ESF, edge spread function; LSF, line spread function derived from ESF. (b) Axial resolution test on a tungsten wire. (c) Photograph of a metal grid. (d) Maximum amplitude projection image

computed from the region enclosed by the red rectangle in (c). (e) B-scan image in the plane highlighted by the blue dashed line in (d).

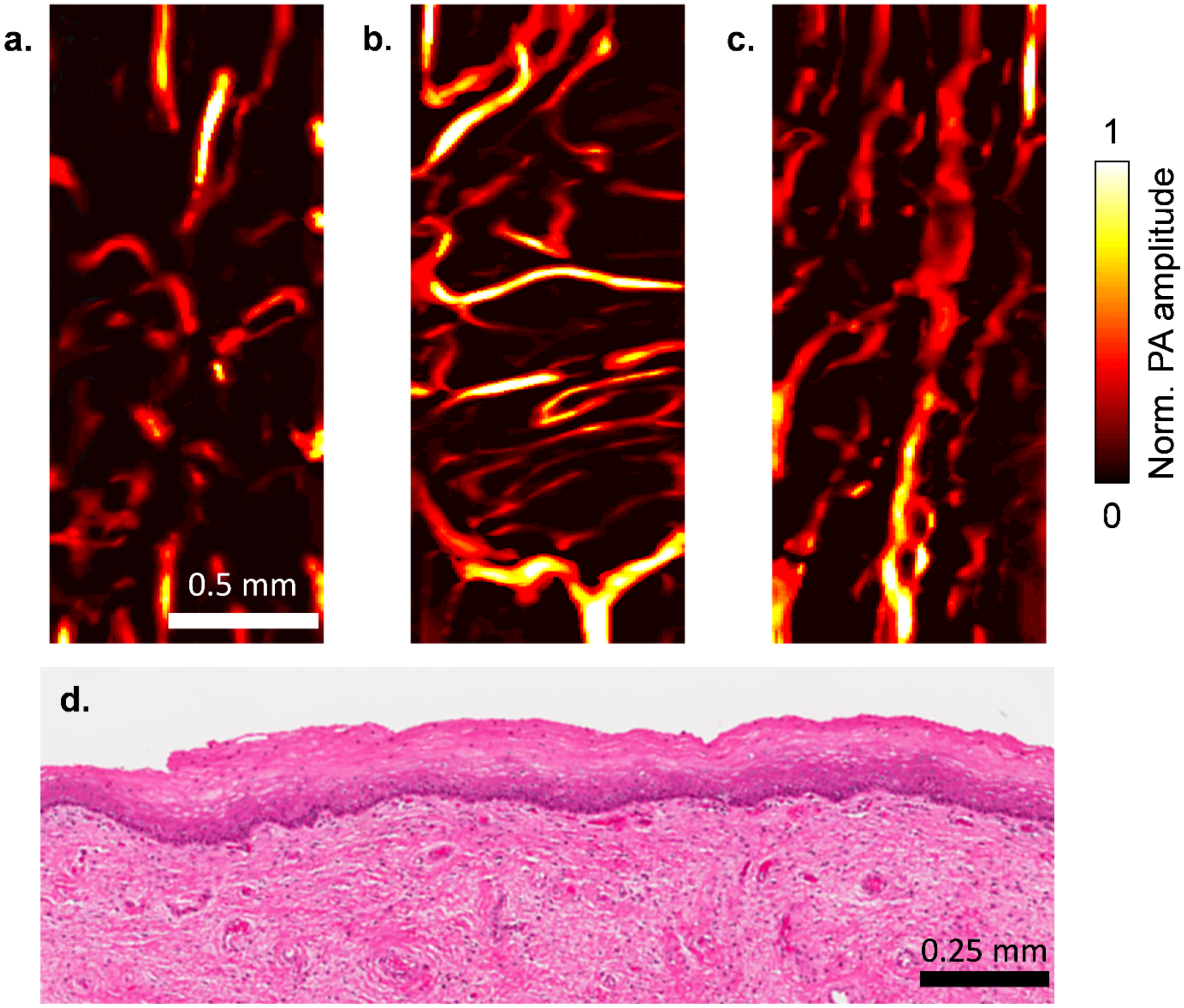

Figure 5.4 *Ex vivo* fsOR-PAE images of (a) the human ectocervix, (b) the serosal layer of the uterine body, and (c) the sublingual mucosa. (d) Standard hematoxylin and eosin histology of the ectocervix conducted after fsOR-PAE imaging, showing no tissue damage.

We then imaged various human tissues to demonstrate the imaging capability of fsOR-PAE. All the human experiments followed protocols approved by the Institutional Review Board administered by the Human Research Protection Office at Washington University in St. Louis.

Ex Vivo Experiment

In an *ex vivo* demonstration, we imaged a uterus obtained from hysterectomy. Figures 5.4(a) and (b) show the vascular networks in the ectocervix and the serosal layers of the uterine body, respectively. A volume-rendered image is shown in Fig. 5.5. Viewed as a projection on the coronal plane, the blood vessels in the ectocervix are more likely to have a small aspect ratio and to be oriented toward the sagittal plane. In addition, the morphology of the vascular network clearly varies from one tissue to another. For example, blood vessels longer than 2 mm are absent in the ectocervix [Fig. 5.4(a)], but these long blood vessels can be easily found in the human sublingual mucosa [Fig. 5.4(c)]. Additionally, we carefully investigated the imaged tissue to demonstrate the safety of fsORPAE. Standard hematoxylin and eosin stain on the imaged area after fsOR-PAE imaging showed no evidence of tissue damage, necrosis, or heat injury [Fig. 5.4(d)].

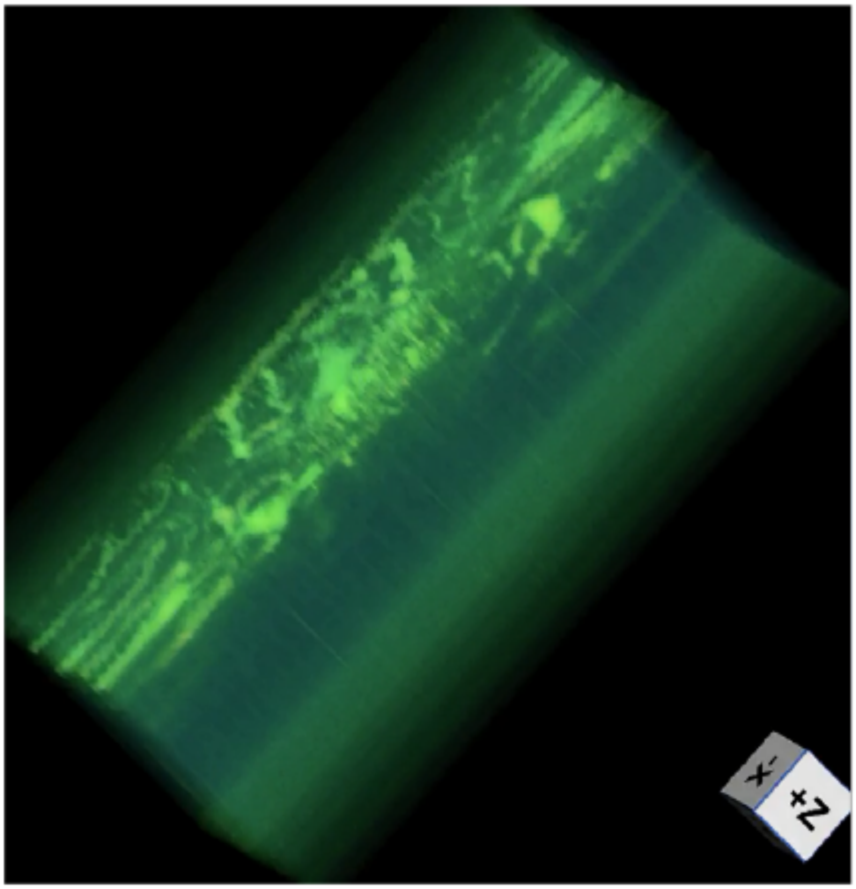

Figure 5.5 Volume-rendered image.

In Vivo Experiment

After we validated the imaging capability and safety of fsOR-PAE, we tested this imaging modality *in vivo* on human subjects. Previous studies found that cervical remodeling during pregnancy was associated with increased vascularity [79,92]. We enrolled (n = 2) pregnant women and imaged the anterior surface of the ectocervix for our study. The first pregnant woman was imaged at 32 weeks of gestation [Fig. 5.6(a)] and again at 36 weeks of gestation [Fig. 5.6(b)]. In this subject, we did not observe a perceptible change of vascular aspect ratio or blood vessel orientation over this time frame. This patient is 30 years old, had two prior deliveries, and had an operative vaginal delivery for nonreassuring fetal status at 39 weeks of gestation in our study. We imaged a second subject to perform a between-subject comparison and noted that blood vessels in the ectocervix of subject 2 had a smaller aspect ratio than in subject 1 at the same gestational age (36 weeks) [Fig. 5.6(c)]. This patient is 24 years old, had one prior delivery, and labored at 38 weeks of gestation in our study.

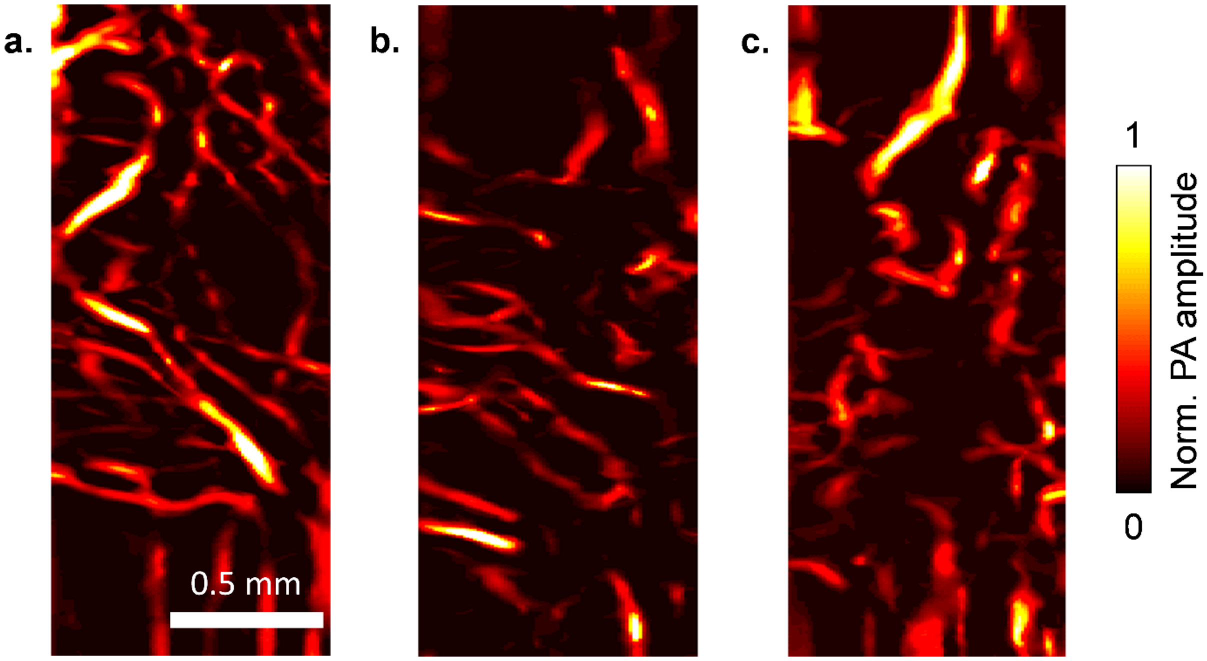

Figure 5.6 *In vivo* fsOR-PAE images acquired from the first pregnant woman at (a) 32 and (b) 36 weeks of gestation. (c) *In vivo* fsORPAE image acquired from the second pregnant woman at 36 weeks of gestation.

To explore what physiological features can be quantified from the fsOR-PAE images, we extrapolate from the two vascular parameters [86] that could have close relationships with cervical remodeling: (1) the microvessel density (the number of vessels per unit area) and (2) total microvascular area (the percentage of area occupied by blood vessels) as shown in Fig. 5.7. Each parameter was calculated from five images measured from different areas. In the analysis, the blood vessels were segmented in three-dimensional (3-D) space, using a threshold set at three times the noise level, estimated as the standard deviation of the background signal outside the imaged region. The segmented outcomes were visually inspected and corrected if necessary. Our results show that the microvessel density is the more promising parameter for identifying the progress of cervical remodeling [Fig. 5.7(a)]. The total microvascular area, however, is a more discriminatory parameter for classifying the type of tissue [Fig. 5.7(b)]. Of course, these conclusions require validation in larger, blinded preclinical studies.

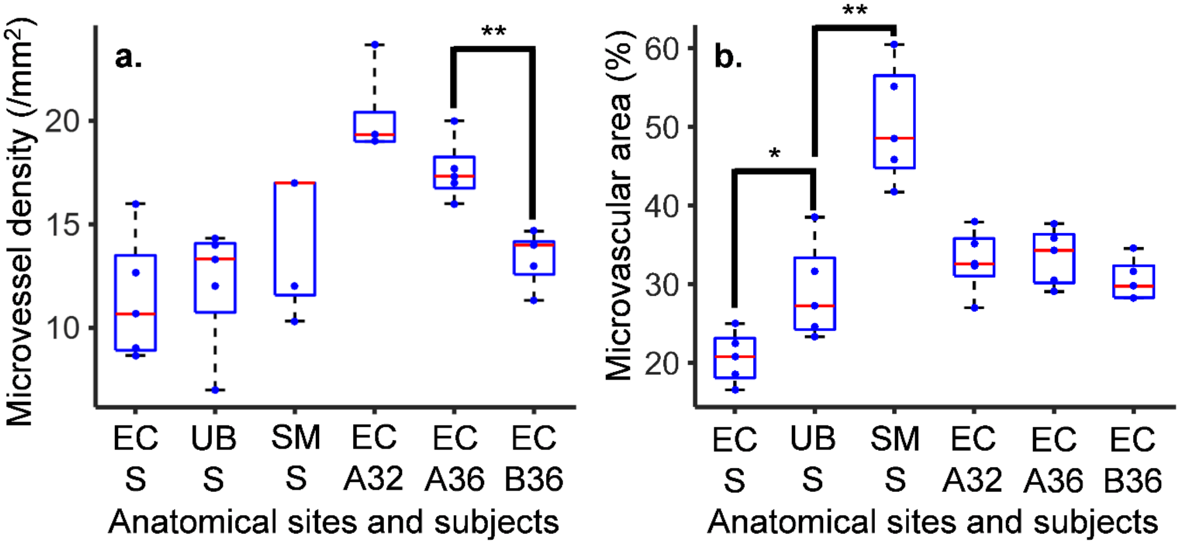

Figure 5.7 Box plots for the histomorphological quantities calculated from the fsOR-PAE images. Five images were analyzed for each subject. (a) Microvessel density and (b) total microvascular area. EC A32, the ectocervix of the first patient at 32 weeks of gestation; EC A36, the ectocervix of the first patient at 36 weeks of gestation; EC B36, the ectocervix of the second patient at 36

weeks of gestation; EC S, the ectocervix specimen; SM S, the sublingual mucosa specimen; UB S, the uterine body specimen. $^{*}P < 0.05$, $^{**}P < 0.01$ in t-tests.

5.4 Discussion

In summary, we have developed an fsOR-PAE system that can achieve a 250-Hz B-scan rate over a 3-mm scanning range. This research presents the first high-resolution in vivo imaging of the vascular network in the human cervix, and its capillary-level spatial resolution is beyond the scope of current clinical methods [88]. Further improvements could include minimizing the size of the probe to reach smaller cavities in the human body and exploiting a dual-wavelength light source to quantify oxygen metabolism [93]. Furthermore, with the development of artificial intelligence, emerging classification models may divulge latent information beyond human recognition, but more valuable for diagnosis than the conventional histomorphological quantities in the fsOR-PAE images [94,95].

Chapter 6: Physiology of Cervical Remodeling during Pregnancy

Cervical remodeling is a necessary step preceding both term and preterm vaginal birth, and it is a critical common pathway linking multiple etiologic factors to spontaneous preterm birth, a leading cause of death among children under 5 years old. Even though preterm birth claimed approximately 1 million lives worldwide in 2015, the physiological pathway behind cervical remodeling is not fully understood. In this chapter, we summarize the physiological processes that we have observed in pregnant women by using photoacoustic techniques over the last three years. The results show that the overall oxygen saturation and vascularity in tissue do not change significantly throughout gestation. In contrast, the increase of tissue hydration is statistically significant. In the end, I will discuss the technical challenges encountered in this study and suggest potential solutions.

6.1 Background

Preterm labor is one of the most serious and unsolved problems in obstetric healthcare. It is a leading cause of death among children under 5 years old and claimed approximately 1 million lives among the 141 million babies born in the world in 2015 [96]. Many factors, such as infection/inflammation, uterine over distension, decreased progesterone, cervical abnormalities, and circadian rhythm disorders, are associated with this syndrome, mainly through three pathways - rupture of membranes, uterine contraction, and cervical remodeling [97]. The mechanisms of these pathways and their relations to etiologic factors have not been fully understood.

This chapter summarizes my research in the last three years on the physiology of cervical remodeling. I used the three photoacoustic endoscopes (PAEs) introduced in the previous chapters. My results show that the overall oxygen saturation and vascularity in tissue do not change significantly throughout gestation. In contrast, the increase in tissue hydration is statistically significant. The chapter concludes with a discussion of the technical challenges encountered in this study and suggests potential solutions.

6.2 Methods

Study Participants

We performed a prospective cohort study of women longitudinally throughout pregnancy. Participants in the preclinical study were recruited from the patient population attending the Obstetrics and Gynecology Clinic and the Women's Health Center in the Barnes-Jewish Hospital Center for Outpatient Health. Eligibility requirements included an age of 18 or older, the capability of informed consent, and a gestational age of enrollment <16 weeks, and singleton gestation. Exclusions included potential participants who were non-English speaking, unwilling to participate, carrying a twin pregnancy, or showing evidence of major fetal anomalies.

Obtaining cervical photoacoustic endoscopy measurements:

A clinically trained obstetric research provider or physician introduced a speculum into the vagina to expose the cervix. Once the cervix had been visualized, the cervical photoacoustic endoscopy probe was placed on the anterior lip of the cervix, with the imaging window downward facing to the anterior cervical tissue (Fig. 6.1). All three probes introduced in Chapter 3, 4, and 5 were used to obtain cervical physiologic data. The operator had real-time feedback for assessment of measurement quality. After the measurement, the speculum was removed from the vagina. All experimental procedures were carried out in accordance with the protocols approved by the Institutional Review Board of Washington University in St. Louis. All participants signed informed consents before inclusion in the study.

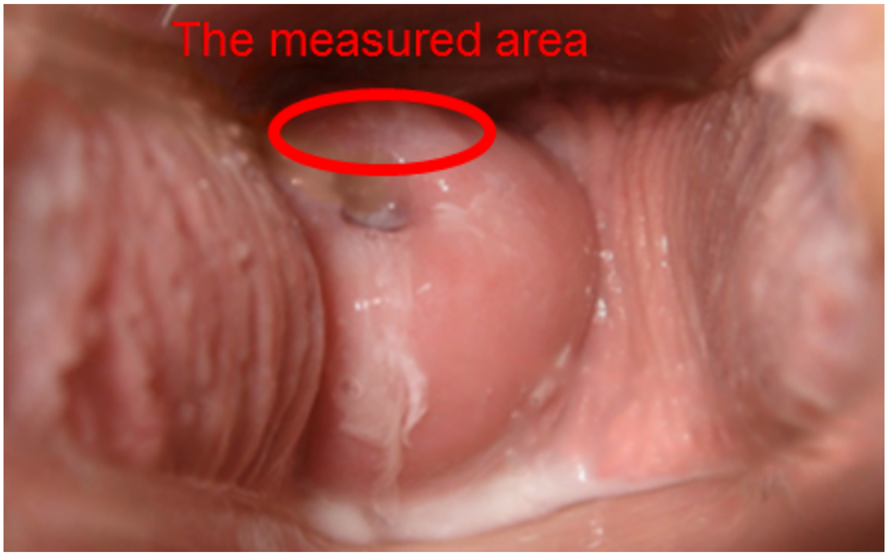

Figure 6.1 Photograph of cervix. The red circle highlights the measured area in our exam. The photograph is copied from *www.beautifulcervix.com*.

As of October 1, 2019, there were 522 participants with delivery data available for analyses. Among these, 442 (85%) had full-term births, whereas 80 (15%) had preterm births, 39 of which were spontaneous preterm births resulting from preterm labor or preterm rupture of membranes.

Calculation of Oxygen Saturation

To calculate the hemoglobin oxygen saturation (sO2) in the blood, we used a conventional method [98], based on the assumption that the dominant absorbing compounds in the visible wavelength range are deoxyhemoglobin (HbR) and oxyhemoglobin (HbO2). Therefore, the blood absorption coefficient $\mu_a(\lambda_i)$ at a wavelength λ_i can be formulated as

$$\mu_a(\lambda_i) = \varepsilon_{\mathrm{HbR}}(\lambda_i)[\mathrm{HbR}] + \varepsilon_{\mathrm{HbO2}}(\lambda_i)[\mathrm{HbO2}]. \tag{6.1}$$

Here, $\varepsilon_{\mathrm{HbR}}(\lambda_i)$ and $\varepsilon_{\mathrm{HbO2}}(\lambda_i)$ are the molar extinction coefficients of HbR and HbO2 at λ_i, respectively. In our experiment, we imaged the tissue at 562 nm and 578 nm. [HbR] and [HbO2] correspond to the concentrations of deoxyhemoglobin and oxyhemoglobin, respectively. The amplitude of the photoacoustic (PA) signal $PA(\lambda_i)$ is proportional to the absorption coefficient $\mu_a(\lambda_i)$ and local light fluence $F(\lambda_i)$. Therefore, the concentrations [HbR] and [HbO2] can be calculated by

$$M = \begin{bmatrix} \varepsilon_{\mathrm{HbR}}(562\,nm) & \varepsilon_{\mathrm{HbO2}}(562\,nm) \\ \varepsilon_{\mathrm{HbR}}(578\,nm) & \varepsilon_{\mathrm{HbO2}}(578\,nm) \end{bmatrix}, \tag{6.2}$$

$$\begin{bmatrix} [\mathrm{HbR}] \\ [\mathrm{HbO2}] \end{bmatrix} = (M^T M)^{-1} M^T \begin{bmatrix} PA(562\,nm) \\ PA(578\,nm) \end{bmatrix} K, \tag{6.3}$$

where *K* is a coefficient relevant to the acoustic properties of the tissue and the local light fluence. Since *K* is unknown in general, the equation can provide only relative concentrations of HbR and HbO2, but these suffice to calculate sO2:

$$\mathrm{sO2} = \frac{[\mathrm{HbO2}]}{[\mathrm{HbR}] + [\mathrm{HbO2}]}. \tag{6.4}$$

In practice, we calculate the sO2 only in regions occupied by blood vessels. To select these regions, we use the AR probe to scan the resolution chart (Fig. 3.2) every day. The image obtained from the resolution chart always contains a blank region above the stripe pattern, because the black stripes are embedded underneath a layer of transparent polymer. A threshold level is set at three times the noise level estimated as the standard deviation of the pixel values in this blank region. In an acoustic-resolution (AR) image acquired *in vivo*, we assume that all the regions in which the pixel values are above the threshold are occupied by blood vessels. Then, we reduced the map of sO2 to a scalar, calculating the average sO2 value over all the occupied regions.

We also note that the calculated sO2 in the entire field of view (FOV) is quantitatively inaccurate, because the AR image can show blood vessels multi-millimeters underneath the tissue surface. In this case, the superficial vessels affect the amount of light that is absorbed by the deep vessels underneath them, and we have not solved the problem of how to estimate the local light fluence in the entire field. Therefore, the sO2 results that we show in this chapter are only qualitatively meaningful.

Calculation of Water Content

To quantify the water content, because the intercorrelation effect of multiwavelength models led to strong instability [51], we fitted a single-wavelength linear regression model based on the empirical calibration. To minimize the correlation between our measurements and any variation in the environment, we collected photoacoustic near-infrared (PANIR) spectra by random sample selection for both the calibration set and the validation set. The calibration set and the validation set each included 350 PANIR spectra, measured from phantoms whose compositions covered the entire range of water contents in soft human tissues (70% to 100%) [64]. Then we applied this model to the spectra measured *in vivo*, based on the assumption that the hydrogel and the cervical connective tissue were so similar that the regression model derived from one could be applied to the other [61-63].

Calculation of Microvessel Density and Total Vascular Area

The blood vessels in the optical-resolution (OR) image are segmented by a global threshold. The threshold level is set at three times the noise level estimated as the standard deviation of the background signal. By tracking the cross-sections of each vessel throughout all the cross-sectional images, we manually label and segment the vessels. The microvessel density corresponds to the number of vessels in a unit area [86], and the total vascular area is equal to the number of pixels above the threshold divided by the number of pixels in the FOV [86].

6.3 Results

Table 6.1 Baseline demographic and clinical characteristics in the analysis of oxygen saturation. Age and body-mass index are examined in the t-tests. The other markers are examined in the Chi-squared tests.

	Preterm (n=10)	**Full-term (n=10)**	***P*-value**

Age – years	31.7±3.7	30.4±4.6	0.49
White race – no. (%)	1 (10)	7 (70)	0.02
Body-mass index	34.7±10.1	26.1±7.3	0.06
Previous full-term delivery – no. (%)	4 (40)	3 (30)	1.00

Change of Oxygen Saturation in the Cervix

In the analysis of how the oxygen saturation in the cervix changes with respect to the delivery outcomes, we selected two groups of participants (Table 6.1), from the entire AR dataset (n = 493). These two small groups corresponded to two opposite and extreme cases for gestation. If any difference concerning cervical oxygen saturation associated with the delivery outcomes existed, such a difference should be shown in the comparison between these two groups. The first group, the preterm group, included ten participants with spontaneous preterm births, and these participants had the shortest gestation in the entire AR dataset. The mean age of the participants with preterm birth was 31.7 years, and the mean body-mass index was 34.7. Four participants had at least one full-term delivery before they joined our study. The second group, the full-term group, included ten participants who had the longest gestation in the entire AR dataset. The mean age of the participants was 30.4 years, and the mean body-mass index was 26.1. Three participants had at least one full-term delivery before they joined our study. In our study, gestation is divided into three periods. The first trimester (T1) is between 1 and 13 weeks of gestation; the second trimester (T2) is between 14 and 26 weeks of gestation; the third trimester (T3) is the period after 26 weeks of gestation.

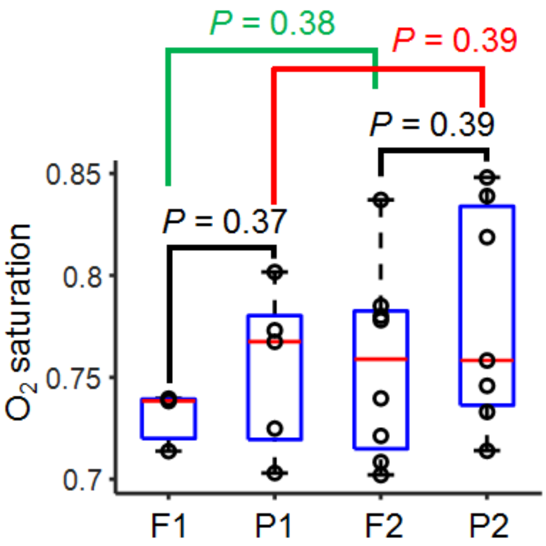

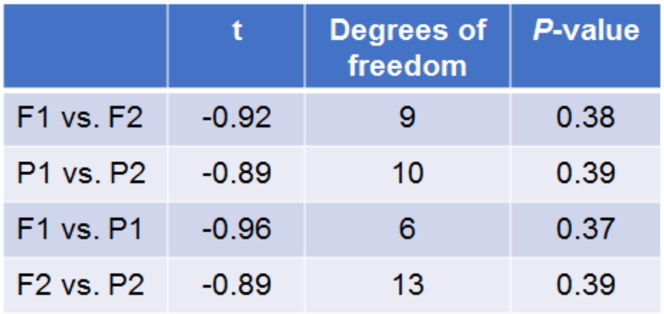

	t	Degrees of freedom	*P*-value
F1 vs. F2	-0.92	9	0.38
P1 vs. P2	-0.89	10	0.39
F1 vs. P1	-0.96	6	0.37
F2 vs. P2	-0.89	13	0.39

Figure 6.2 A box plot for the average sO2 value measured in each study visit. F1, the full-term group in the first trimester; P1, the preterm group in the first trimester; F2, the full-term group in the second trimester; P2, the preterm group in the second trimester. The statistical results are shown on the right.

In this analysis, we reduced the two-dimensional map of sO2 in tissue to a scalar, the average value of sO2 in tissue (Fig. 6.2). Since none of the participants in the preterm group had a study visit in their third trimester, we focused on the first two trimesters. First, the average sO2 values do not differ between T1 and T2, with respect to either the full-term group ($P = 0.38$) or the preterm group ($P = 0.39$) by the Student's t-test. Second, the average sO2 values in neither trimester ($P = 0.37$ in T1 and $P = 0.39$ in T2) show a statistical difference between two groups of patients by the Student's t-test.

Change of Tissue Hydration in the Cervix

Table 6.2 Baseline demographic and clinical characteristics in the analysis of tissue hydration. Age and body-mass index are examined in the t-tests. The other markers are examined in the Chi-squared tests.

	Whole group (n=295)	**Preterm (n=44)**	**Full-term (n=251)**	***P*-value**
Age – years	29.8±5.3	30.0±6.2	29.8±5.2	0.81
White race – no. (%)	128 (43)	16 (36)	112 (45)	0.39
Body-mass index	28.7±8.4	31.4±9.8	28.3±8.1	0.02
Hypertension that predates conception – no. (%)	20 (7)	6 (14)	14 (6)	0.10
Diabetes mellitus – no. (%)	19 (6)	7 (16)	12 (5)	0.01
Previous full-term delivery – no. (%)	150 (51)	17 (39)	133 (53)	0.11
Previous preterm delivery – no. (%)	31 (11)	8 (18)	23 (9)	0.12

In the first step, we compared our data with a biochemical study [70]. Our data set was measured from 295 participants who had more than one study visit and had delivery outcomes available before Oct. 1, 2019 (Table 6.2). The mean age of the participants was 29.8 years, and the mean body-mass index was 28.7. In this group, 128 participants were white, 31 participants had at least one preterm delivery before they joined the study, and 44 participants had a preterm delivery during this study. Ref. 70 indicates that cervical hydration in non-pregnant women is about 75% (±7%) and cervical hydration at the end of gestation is about 81% (±5%). The distribution of water contents measured in our study is shown in Fig. 6.3. The mean value is 77%, with a standard deviation 6%, which is consistent with a previously reported study [70].

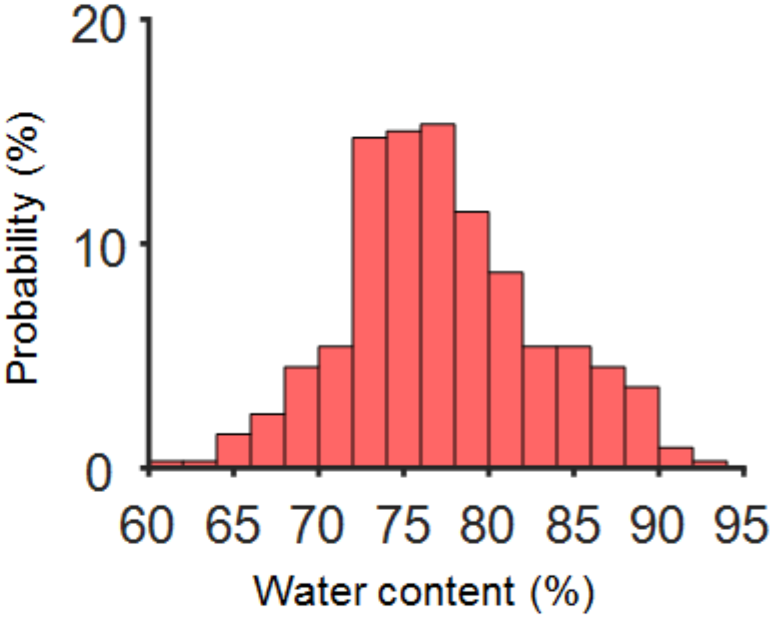

Figure 6.3 Distribution of water contents measured from pregnant women in this study (n=295).

After we confirmed the consistency of our data set with the biochemical study, we divided our data set into two subsets - a preterm group and a full-term group - based on the clinical outcomes. (Table 6.2). We then applied a generalized linear model [71] in the preliminary analysis. We observed serial and cross-sectional changes in the measured cervical hydration in pregnancy (Fig. 6.4). The rate of cervical hydration increase in the preterm labor group is 0.35% per week, significantly higher than the 0.21% per week in the full-term labor group (*P* = 0.03). The progressive increase of cervical hydration until delivery suggests a slow longitudinal maturation of the cervix over the duration of the pregnancy, and this observation is also consistent with the biochemical study [70].

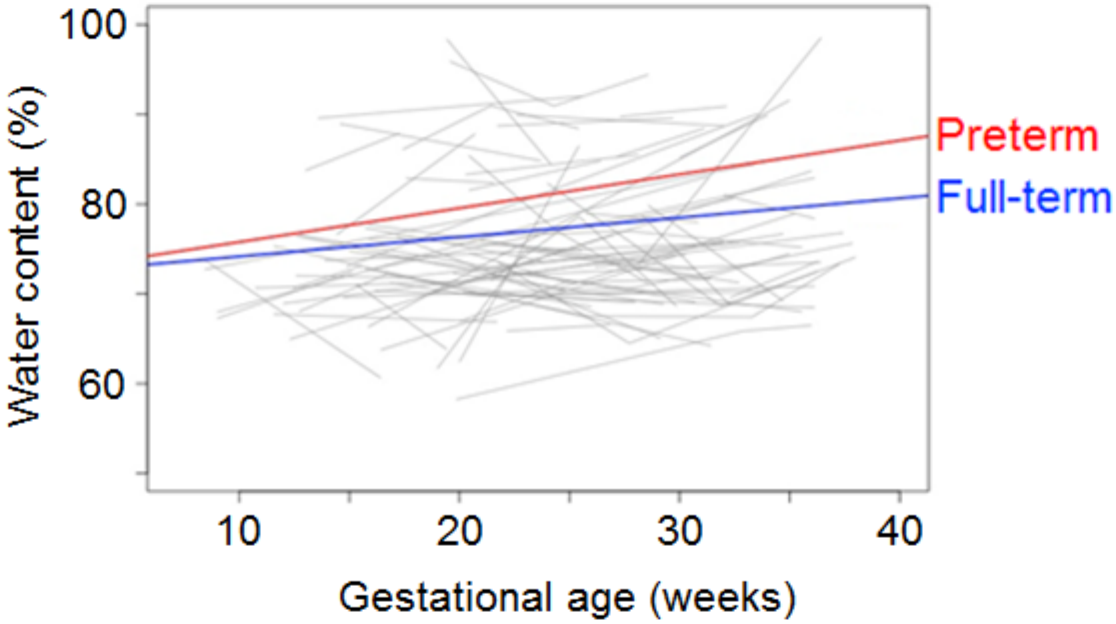

Figure 6.4 Longitudinal changes of water contents in the cervixes of pregnant women (n = 295), shown as gray lines. The red solid line indicates the fit at the unit level of the generalized linear model to the data from the preterm group (n = 44), and the rate of cervical hydration increase is 0.35% per week. The blue solid line indicates the fit to the data from the full-term group (n = 251), and the rate of increase is 0.21% per week.

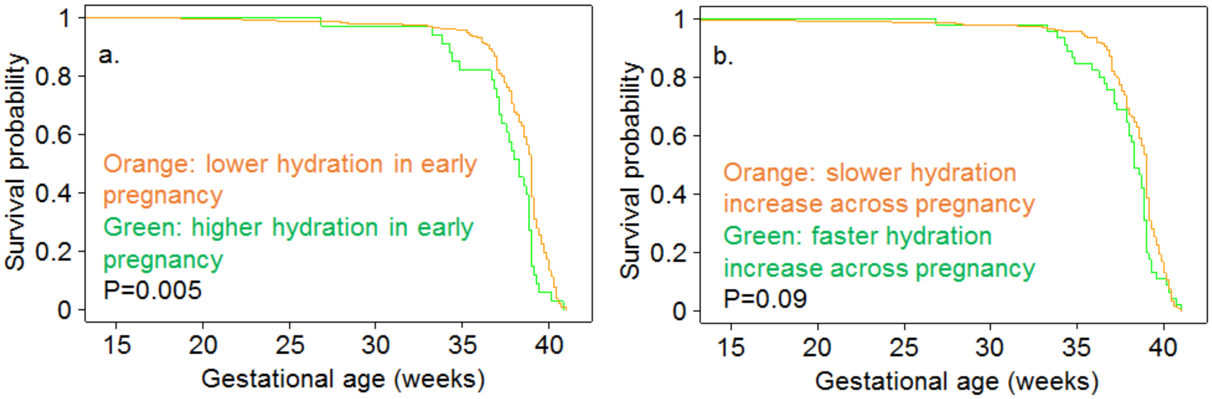

Figure 6.5 Survival analysis for the pregnant women (n = 295) with respect to their cervical hydration. The intercept and slope for each woman were obtained from the generalized linear model. (a) Two groups are separated with respect to the intercept. (a) Two groups are separated with respect to the slope. A higher hydration in early pregnancy is significantly associated with shorter gestational length. A faster increase in cervical hydration approaches, but does not reach, statistical significance for shorter gestation.

In the survival analysis based on the generalized linear model, we tested two hypotheses. First, our results suggest that the detectable difference in cervical hydration in early pregnancy was associated with shorter gestational length (Fig. 6.5a). In this test, we separated the low intercept group and high intercept group at 85% water content, where we obtained the strongest statistical evidence to support the first hypothesis. Second, although a fast increase in the cervical hydration (slope) is also correlated with early termination of gestation (Fig. 6.5b), no matter how we separate the two groups with respect to the slope, the statistical result is always insignificant in the survival analysis. We note that detectable differences in cervical hydration in early pregnancy are clinically appealing, because the measurement is easily obtainable in early obstetric visits, and early detection is most useful for applying prevention strategies and performing risk stratification of patients.

Table 6.3 Baseline demographic and clinical characteristics of the groups in the analysis of vascular morphology. T1, first trimester; T2, second trimester; T3, third trimester; F2, second trimester measurement, subsequent full-term delivery; P2, second trimester measurement, subsequent preterm delivery; F3 third trimester measurement, subsequent full-term delivery; P3, third trimester measurement, subsequent preterm delivery.

	T1 (n=3)	**T2 (n=16)**	**T3 (n=31)**	**F2 (n=13)**	**P2 (n=4)**	**F3 (n=24)**	**P3 (n=7)**
Age – years	26.0±5.6	30.4±4.9	29.7±4.5	31.1±4.7	28.3±5.9	29.9±4.4	29.0±5.2
White race – no. (%)	1 (3)	8 (50)	13 (42)	7 (54)	1 (25)	11 (46)	2 (29)
Body-mass index	28.3±6.8	30.1±11.4	29.5±8.4	31.7±11.9	25.1±9.1	28.6±8.1	31.7±9.4
Previous full-term delivery – no. (%)	1 (33)	10 (63)	15 (48)	8 (62)	2 (50)	13 (54)	2 (29)

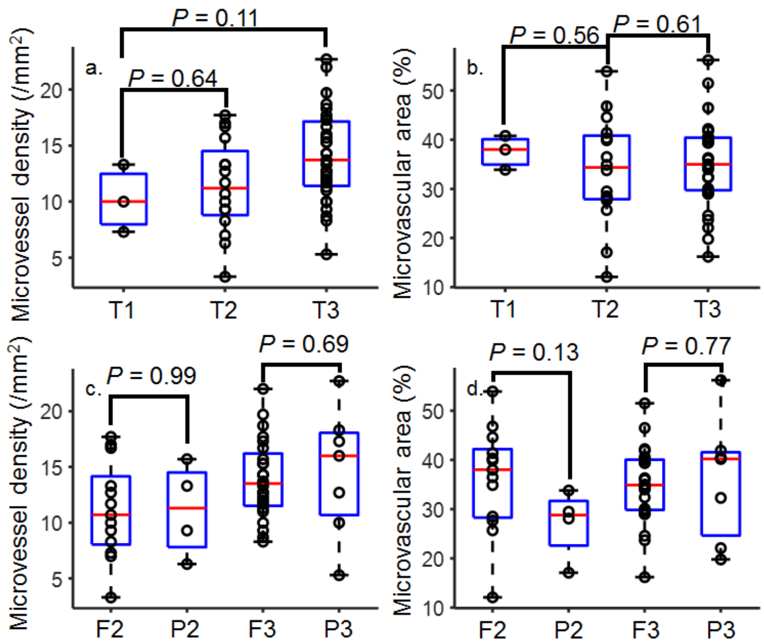

	t	Degrees of freedom	*P*-value
T1 vs. T2 Density	-0.47	17	0.64
T1 vs. T3 Density	-1.61	32	0.11
T1 vs. T2 Area	0.58	17	0.56
T2 vs. T3 Area	-0.51	45	0.61
F2 vs. P2 Density	0.00	15	0.99
F3 vs. P3 Density	-0.40	29	0.69
F2 vs. P2 Area	1.57	15	0.13
F3 vs. P3 Area	-0.29	29	0.77

Figure 6.6 Box plots for the histomorphological quantities calculated from the OR-PAE images. (a) Microvessel density and (b) total microvascular area with respect to gestation progress. T1, first trimester; T2, second trimester; T3, third trimester. (c) Microvessel density and (d) total microvascular area with respect to delivery outcomes. F2, full-term delivery in the second trimester; P2, preterm delivery in the second trimester; F3 full-term delivery in the third trimester; P3, preterm delivery in the third trimester. The statistical results are shown on the right.

Change of Vascular Morphology

In the analysis of vascular morphology, from the entire OR data set (n=389), we selected the measurements from 37 participants who had 51 study visits in total (Table 6.3). Two exclusion criteria were applied: (1) a contrast-to-noise ratio of less than 3 and (2) the existence of misalignment artifacts. The mean age of the participants was 29.7 years, and the mean body-mass index was 30.5. Eighteen participants were white, twenty-one participants had at least one full-term delivery before they joined our study, and ten participants delivered preterm in this study.

We tested whether microvessel density and total microvascular area have the power to identify the progress of cervical remodeling or to predict the delivery outcome. We plotted these parameters in box plots under different classifications (Fig. 6.6). The microvessel density shows a slight increase throughout gestation, but the increase is statistically insignificant by the Student's t-tests (Fig. 6.6a). In comparison, the total microvascular area does not show an upward trend across the trimesters (Fig. 6.6b). These two plots in combination imply that the vascular network is more likely to contain more bifurcations at the end of gestation than at the beginning. When we also considered the delivery outcome of participants and distinguished the preterm group from the full-term group, the microvessel densities measured from the two groups in the same trimester were distributed in the same range, as were the total microvascular areas.

6.4 Discussion

In this primary analysis for our cervical remodeling study using PAEs, we observed a significant change of cervical hydration, but the vascular morphology and the overall oxygen saturation did not show significant changes. By comparing the cervical hydration, we successfully classified a group of patients whose gestation was likely to terminate early. This result is encouraging, because the measurement is easily obtainable in the early obstetric visits. Early detection is the most useful for applying prevention strategies and stratifying patients.

The PA techniques that we developed for this study are still in their primary stage. In the last three years, we encountered numerous challenges that should be addressed in the next phase.

The first challenge is the complicated mechanisms involved in preterm birth. Preterm labor is associated with three different physiological processes [97]: uterine contraction, rupture of the chorioamniotic membrane, and cervical dilation. An abnormality in any one of these processes can trigger preterm labor. Our methodology detects only cervical remodeling physiology which may not be an etiologic factor in all preterm births. In our analysis, all patients with a spontaneous preterm birth were classified into the preterm group, and the specific causes of their preterm birth were neglected because of the small number of patients in the preterm groups with cervical dilation - the only variable that our techniques can monitor. In the next stage, the study should recruit more patients with a high risk of preterm birth, based on patients' medical records.

In addition, we stratified our analysis by trimesters, which are arbitrary units of time and do not necessarily correlate with cervical physiology in an ordered categorical fashion. Instead, it would be more useful to examine the change of physiology continuously over gestation. Categorization by trimesters may have made some physiologic phenomena more difficult to detect.

In terms of the hardware, we need to reduce the 20 mm diameter of our endoscopes. In a study visit, prior to measuring the cervix, the operator must place a speculum in the vagina, exposing the cervix for endoscopy. Once an endoscope has been moved into the vagina, the operator can no longer visualize the cervix because it is blocked by the endoscope. This visual blockage is not very important for the AR probe, because it has a large FOV (7 mm × 6 mm) and the operator can adjust the position of the probe based on the AR images shown by the computer in real-time. This same task, however, is not easy with the other two probes. The PANIR probe measures the spectrum from a single point. Although our assessment program (Fig. 4.2) can provide measurement quality feedback for the operator, this limited information cannot illustrate how the operator should move the probe to improve the measurement quality. The story is similar for the OR probe, which has a FOV of 3 mm × 1 mm × 1 mm, smaller than that of the AR probe. If blood vessels are outside the FOV of the OR probe at the beginning, the operator will have to blindly search the imaging spot. Our participants also often reported discomfort in the process of adjustment. Ideally, an endoscope with a diameter smaller than 10 mm would allow the operator to see the cervix and the probe simultaneously in the vagina.

How we injected distilled water into the AR and OR probes also needs to be improved. To protect the transducer from degrading, every day we drained the water from the probe after the last exam and re-injected new water into the probe before the first exam on the next day. Air bubbles were often trapped in the probe in this procedure. As a result, when people moved the probe throughout the day, the air bubbles also moved inside the probe. Sometimes the air bubbles attached on the surface of the transducer, which affected the detection sensitivity of the probe. If the sensitivity changes exam by exam, the PA amplitudes measured from different patients cannot be compared directly, because a small PA amplitude may be associated with a low detection sensitivity rather than the patient's physiology. So far, we have tried injecting water through micro tubing from both the top and the bottom of the probe, and neither position can guarantee that the chamber in the probe will be free from air bubbles after water injection. Potential solutions for this problem could involve (1) coating the surface of the transducer with a hydrophilic layer, (2) changing the geometry of the probe so that all air bubbles are ejected from the probe in the process of water filling, or (3) once there are no bubbles in the probe, leaving the water in the probe permanently.

In the analysis of the sO2 data measured by the AR probe, we realized two factors could lead to inaccuracy. The first factor is the physiology of our participants. Our participants had various genetic backgrounds, and many studies have shown that genetic characteristics give rise to differences in tissue microstructures [99], influencing how photons propagate in the tissue [100]. Moreover, the process of cervical remodeling itself also changes the tissue microstructure [81]. In this process, the collagen fibers in the extracellular matrix are aligned and straight at the early stage of gestation. Later in the gestation, the fibers became more disordered, which changes the scattering effect as well as the distribution of light fluence in the entire FOV. The second factor relates to how the operator uses the probe. Five operators acquired the data in this study. When an operator puts the imaging window on the cervix, the tissue is inevitably pressed and deformed. This deformation also changes the environment in which the photons propagate. We do not yet have a mechanism to quantitatively monitor the amount of pressure applied on the cervix, so operator variability remains as a possible source of inaccuracy.

A few potential solutions could solve the problems in sO2 measurement. The deeper the light propagates, the more influence the environment has on the light fluence, so using the OR probe to measure the sO2 is a potential solution to mitigate this uncertainty. Also, a tabletop PA system has been demonstrated to measure sO2 with a fiber laser [93], and that design can be adopted by upgrading the current OR system. To address the variation caused by tissue deformation, the next generation probe could include a pressure sensor near the imaging window, so the operator can control the applied pressure as well as the degree of tissue deformation with feedback from the sensor. With accurate pressure control, measurements of sO2 should be more consistent over time.

We also recognized two major drawbacks in the current PANIR system. The first drawback relates to the probe cover that must be used in the exam, required by the disinfection protocol. We used a polyethylene probe cover (Eclipse, Parker Laboratories). Polyethylene itself is routinely used in near-infrared spectral analysis [101], but the ultrasound transmission gel inside the probe cover is a highly absorptive substance in the near-infrared wavelength range and causes a serious problem. The probe cover is large, with a lot of room inside for the PANIR probe to move, and the operator cannot guarantee that no ultrasound gel has moved between the probe window and the tissue in the exam. Although the algorithm that we developed (Fig. 4.2) can provide the operator with measurement data quality during the exam, the considerable number of failures caused by the ultrasound gel cannot be reduced as long as we use the current probe cover. Potential solutions for this problem could be (1) a new disinfection method which makes the probe cover unnecessary or (2) a new probe cover customized for the geometry of our probes, so no ultrasound gel can get between the probe window and the tissue.

The second drawback relates to the instability of the impulse response of the PANIR probe. The instability originates from our probe design, in which we use a N-BK7 pentaprism so that near-infrared light propagates through a transparent medium before being absorbed by the tissue. The other conventional media used in PA systems, such as water, absorb light in the near-infrared range. If the PA signal generated from the medium is dominant in the data, the probe will lose its ability to quantify tissue hydration. The pentaprism, however, has an acoustic impedance much larger than those of tissue and air, and such a mismatch undesirably creates an acoustic cavity. The acoustic wave propagating from the tissue to the transducer is localized in the cavity for a while. The shape of the wave detected by the transducer is the result of the interference of acoustic waves reflected from different surfaces, and the interference is nonlinear. As a result, the impulse response of the probe is very sensitive to the contact between the tissue and the probe window, so a perturbation can significantly distort the waveform (Fig. 4.2). The theoretical details of the instability can be found in Ref. 103. A potential solution for this problem is to modify the PANIR probe and adopt a design similar to the AR probe. Of course, distilled water cannot be used as the medium in which the light and the acoustic wave propagate. Fortunately, deuterium oxide, D_2O, is transparent in the near-infrared range and has an acoustic impedance close to that of tissue. The results measured by the PANIR probe with the new design may be more precise and more stable over time. This improvement may be important for analyzing the relationship between the tissue hydration and various etiologic factors.

We found two additional problems when we tried to use more sophisticated machine learning techniques to analyze the OR results. Fig. 6.7 illustrates one problem. Fig. 6.7a and b were measured in one exam. Their imaging spots are different; however, the vascular morphologies still look quite similar, in terms of the vascular diameter and orientation. Fig. 6.7c and d were measured in one exam for another patient. Again, their imaging spots are different, but Fig. 6.7c and d show two different orientations. If we use a deep learning method to classify the OR images, we must carefully track the features in the neural network. When the features used as criteria for classification include the vascular orientation, an undesired overfitting occurs in training the neural network. In future preclinical studies, people also need to design a plan for multiple sampling locations on the cervix, to reduce the data variance due to inhomogeneous sampling in the data set.

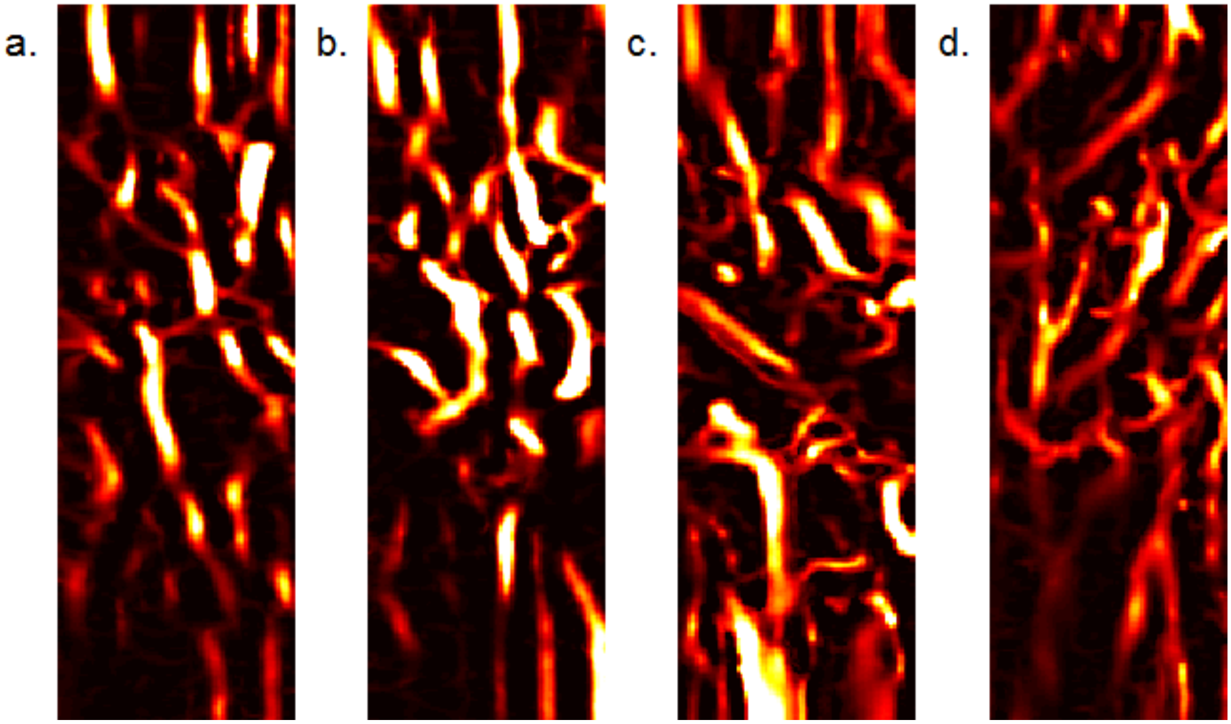

Figure 6.7 The effect of imaging location on OR-PAE images. (a and b) *In vivo* OR-PAE images acquired from a pregnant woman in one exam. (c and d) *In vivo* OR-PAE images acquired from another pregnant woman in one exam. The conclusion that we draw from the OR-PAE images, for example, regarding vascular orientation, depends on the imaging location.

The second problem that we found is also associated with the pressure applied on the cervix in the measurement. Fig. 6.8 shows an example. Based on the structures highlighted in the green circles, we can tell that two images were acquired from the same location, however, the maps of PA amplitudes in the two images are quite different. The most prominent vessel in Fig. 6.8a occupies the top left corner, and this vessel is absent in Fig. 6.8b. One possible explanation for this difference is that less pressure was applied on the cervix when Fig. 6.8a was acquired. The most prominent vessel was closer to the surface of cervix than the other vessels in the image. When Fig. 6.8b was acquired, the operator applied more pressure in the area highlighted in the green circle. In this case, the blood originally inside the prominent vessel shown in Fig. 6.8a was squeezed out so that this vessel disappeared when Fig. 6.8b was acquired. To address this issue, a pressure sensor should be integrated into the OR probe so that the operator can adjust the pressure.

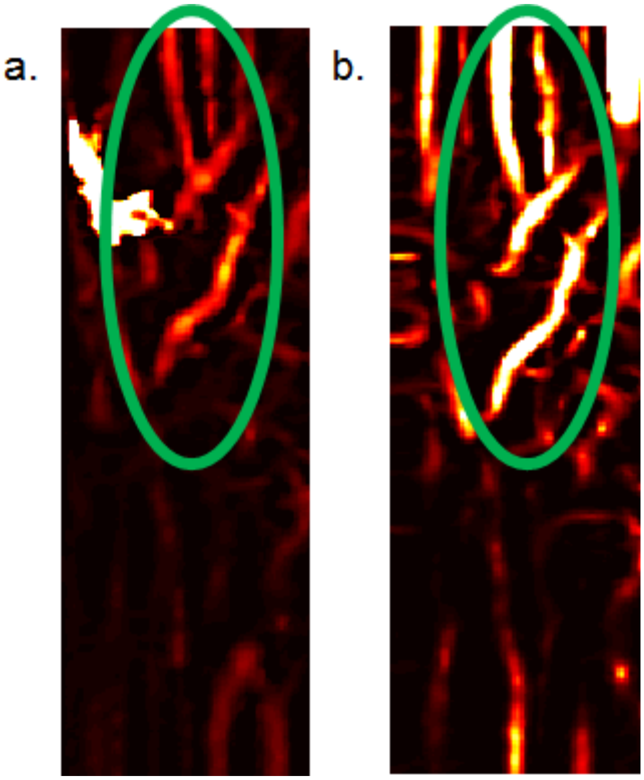

Figure 6.8 The effect of pressure on the OR-PAE images. (a and b) *In vivo* OR-PAE images acquired from a pregnant woman in one exam. The two images were acquired from the same area of the tissue, but the maps of PA amplitude are quite different.

Due to these practical problems mentioned above, we could not use all the data that we collected from the participants in the data analyses. First, the AR measurements were very successful in imaging the cervical tissue. However, in some cases the AR probe was too short to reach the cervix, and sometimes the patient could not tolerate the speculum. Although the measurement success rate is very high (~99%), we have not established a useful prediction model to associate the AR results with the delivery outcomes. The data scientists in our group are trying to build a prediction model based on deep learning. This new model might require higher AR measurement quality, which might lead to a lower measurement success rate. Second, the IR measurements have only a moderate measurement success rate (~40%), and substantial changes of the IR probe and probe cover may be necessary to improve this number. Third, the OR measurements have a low measurement success rate (~15%). In our data analysis, ~50% of the OR images were excluded by the contrast-to-noise ratio criterion, and ~35% of then OR images were excluded by the misalignment artifact criterion.

In conclusion, using photoacoustic techniques, we observed several physiological changes among pregnant women in our three-year study. The overall oxygen saturation and vascularity in cervical tissue did not change significantly throughout gestation. In contrast, an increase of tissue hydration was statistically significant.

Chapter 7: Summary

In this dissertation, we have demonstrated four new photoacoustic techniques for imaging and spectroscopy. DS-PACT can image anisotropic tissue without labels. AR-PAE can provide a qualitative map of oxygen saturation in the cervix. PANIR spectroscopy can quantify tissue hydration. fsOR-PAE can image the superficial vascular network in tissue.

In Chapter 2, we showed that DS-PACT can measure both the amplitude of tissue's dichroism and the orientation of the optic axis of uniaxial dichroic tissue. By modulating the polarization of linearly polarized light and measuring the alternating signals through lock-in detection, DS-PACT can boost dichroic signals from biological tissues. The result has been published on Optica [107].

In Chapter 3, we developed an acoustic-resolution PAE. The side-scanning photoacoustic probe is 20 mm in diameter and has ~10 Hz B-scan rate. Using this device, we acquired *in vivo* experimental results which suggest its potential for comprehensive clinical applications.

In Chapter 4, we demonstrated how to quantify tissue hydration *in vivo*, using the near-infrared spectrum measured by our PANIR system. Applying this method to pregnant women *in vivo*, we observed an increase in the water content of the cervix throughout pregnancy. The application of this technique in maternal healthcare may advance our understanding of cervical remodeling. The result has been published on Journal of Biomedical Optics [108].

In Chapter 5, we presented a transvaginal fast-scanning optical-resolution photoacoustic endoscope with a 250 Hz B-scan rate over a 3 mm scanning range. Using this modality, we not only illustrated morphological differences of vasculatures among the human ectocervix, uterine body, and sublingual mucosa, but also showed longitudinal and cross-sectional differences of cervical vasculatures in pregnant women. The result has been published on Journal of Biomedical Optics [109].

In Chapter 6, we presented the preliminary analysis of a data set acquired by our PAE devices from pregnant women recruited in the March of Dimes 1000 cohort study at the Barnes-Jewish Hospital Center for Outpatient Health. The results showed that the overall oxygen saturation and vascularity in tissue did not change significantly throughout gestation. In contrast, an increase of tissue hydration was statistically significant.

Overall, PAE introduces new possibilities for biomedical applications. For example, the OR-PAE probe, in combination with transgenic microorganisms, can be used for longitudinal monitoring of microbial dynamics in the vagina [15, 104, 105]. Shifting the wavelength range from the near-infrared to the mid-infrared, the IR probe can provide more chemical information in the vagina [106].

References/Bibliography/Works Cited

[1] R. Stadhouders, G. J. Filion, and T. Graf, "Transcription factors and 3D genome conformation in cell-fate decisions," *Nature* **569**, 345–354 (2019).

[2] E. Betzig, G. H. Patterson, R. Sougrat, O. W. Lindwasser, S. Olenych, J. S. Bonifacino, M. W. Davidson, J. Lippincott-Schwartz, H. F. Hess, "Imaging Intracellular Fluorescent Proteins at Nanometer Resolution," *Science* **313**, 1642-1645 (2006).

[3] D. Li, L. Shao, B. Chen, X. Zhang, M. Zhang, B. Moses, D. E. Milkie, J. R. Beach, J. A. Hammer, M. Pasham, T. Kirchhausen, M. A. Baird, M. W. Davidson, P. Xu, E. Betzig, "Extended-resolution structured illumination imaging of endocytic and cytoskeletal dynamics," *Science* **349**, 944 (2015).

[4] H. H. Barrett and K. J. Myers, *Foundations of Image Science* (John Wiley & Sons, 2004).

[5] L. V. Wang and J. Yao, "A practical guide to photoacoustic tomography in the life sciences," *Nature Methods* **13**, 627–638 (2016).

[6] J. Weber, P. C. Beard, and S. E. Bohndiek, "Contrast agents for molecular photoacoustic imaging," *Nature Methods* **13**, 639–650 (2016).

[7] M. Mahendroo, "Cervical remodeling in term and preterm birth: insights from an animal model," *Reproduction* **143**, 429-438 (2012).

[8] V. Talman and H. Ruskoaho, "Cardiac fibrosis in myocardial infarction—from repair and remodeling to regeneration," *Cell Tissue Res.* **365**, 563–581 (2016).

[9] J. A. Joyce and J. W. Pollard, "Microenvironmental regulation of metastasis," *Nat. Rev. Cancer* **9**, 239–252 (2009).

[10] A. B. Roberts, M. B. Sporn, R. K. Assoian, J. M. Smith, N. S. Roche, L. M. Wakefield, U. I. Heine, L. A. Liotta, V. Falanga, J. H. Kehrl, and A. S. Fauci, "Transforming growth factor type β: Rapid induction of fibrosis and angiogenesis *in vivo* and stimulation of collagen formation *in vitro*," *PNAS* **83**, 4167-4171 (1986).

[11] M. F. Penet, B. Krishnamachary, Z. Chen, J. Jin, and Z. M. Bhujwalla, "Molecular imaging of the tumor microenvironment for precision medicine and theranostics," *Adv. Cancer Res.* **124**, 235–256 (2014).

[12] M. Lakshman and A. Needles, "Screening and quantification of the tumor microenvironment with micro-ultrasound and photoacoustic imaging," *Nat. Methods* **12**, iii–v (2015).

[13] L. V. Wang and S. Hu, "Photoacoustic tomography: *in vivo* imaging from organelles to organs," *Science* **335**, 1458–1462 (2012).

[14] J. Yao, L. Wang, J. Yang, K. Maslov, T. T. W. Wong, L. Li, C. Huang, J. Zou, and L. V. Wang, "High-speed label-free functional photoacoustic microscopy of mouse brain in action," *Nat. Methods* **12**, 407–410 (2015).

[15] J. Yao, A. A. Kaberniuk, L. Li, D. M. Shcherbakova, R. Zhang, L. Wang, G. Li, V. V. Verkhusha, and L. V. Wang, "Multiscale photoacoustic tomography using reversibly switchable bacterial phytochrome as a near-infrared photochromic probe," *Nat. Methods* **13**, 67–73 (2016).

[16] S. Hu, K. Maslov, P. Yan, J. Lee, and L. V. Wang, "Dichroism optical resolution photoacoustic microscopy," *Proc. SPIE* **8223**, 82233T1 (2012).

[17] L. Li, J. Xia, G. Li, A. Garcia-Uribe, Q. Sheng, M. A. Anastasio, and L. V. Wang, "Label-free photoacoustic tomography of whole mouse brain structures *ex vivo*," *Neurophotonics* **3**, 0350011 (2016).

[18] G. Li, L. Li, L. Zhu, J. Xia, and L. V. Wang, “Multiview Hilbert transformation for full-view photoacoustic computed tomography using a linear array,” J. Biomed. Opt. 20, 066010 (2015).

[19] P. Zhang, L. Li, L. Lin, P. Hu, J. Shi, Y. He, L. Zhu, Y. Zhou, and L. V. Wang, “High-resolution deep functional imaging of the whole mouse brain by photoacoustic computed tomography *in vivo*,” *J. Biophoton.* **11**, c201700024 (2018).

[20] L. Li, L. Zhu, C. Ma, L. Lin, J. Yao, L. Wang, K. Maslov, R. Zhang, W. Chen, J. Shi, and L. V. Wang, “Single-impulse panoramic photoacoustic computed tomography of small-animal whole-body dynamics at high spatiotemporal resolution,” *Nat. Biomed. Eng.* **1**, 0071 (2017).

[21] J. Xia, M. R. Chatni, K. Maslov, Z. Guo, K. Wang, M. A. Anastasio, and L. V. Wang, “Whole-body ring-shaped confocal photoacoustic computed tomography of small animals *in vivo*,” *J. Biomed. Opt.* **17**, 0505061 (2012).

[22] G. Marriott, S. Mao, T. Sakata, J. Ran, D. K. Jackson, C. Petchprayoon, T. J. Gomez, E. Warp,O. Tulyathan, H. L. Aaron, E. Y. Isacoff, and Y. Yan, “Optical lock-in detection imaging microscopy for contrast-enhanced imaging in living cells,” *PNAS* **105**, 17789–17794 (2008).

[23] American National Standards Institute, “American National Standard for the safe use of lasers,” ANSI Z136.1-2007 (American National Standards Institute, 2000).

[24] M. A. Anastasio, J. Zhang, X. Pan, Y. Zou, G. Ku, and L. V. Wang, “Half-time image reconstruction in thermoacoustic tomography,” *IEEE Trans. Med. Imaging* **24**, 199–210 (2005).

[25] L. V. Wang and H. Wu, *Biomedical Optics: Principles and Imaging* (Wiley, 2007).

[26] M. Born and E. Wolf, *Principles of Optics,* 7th ed. (Cambridge University, 1999).

[27] M. Todorović, S. Jiao, L. V. Wang, and G. Stoica, “Determination of local polarization properties of biological samples in the presence of diattenuation by use of Mueller optical coherence tomography,” *Opt. Lett.* **29**, 2402–2404 (2004).

[28] R. N. Bracewell, *The Fourier Transform and its Applications,* 3rd ed. (McGraw-Hill, 2000).

[29] M. Lee and V. Vasioukhin, “Cell polarity and cancer-cell and tissue polarity as a non-canonical tumor suppressor,” *J. Cell Sci.* **121**, 1141–1150 (2008).

[30] V. Backman, R. Gurjar, K. Badizadegan, I. Itzkan, R. R. Dasari, L. T. Perelman, and M. S. Feld, “Polarized light scattering spectroscopy for quantitative measurement of epithelial cellular structures in situ,” *IEEE J. Sel. Top. Quantum Electron*. **5**, 1019–1026 (1999).

[31] S. A. Cannistra and J. M. Niloff. "Cancer of the uterine cervix," *N. Engl. J. Med.* **334**, 1030–1038 (1996).

[32] J. Yang, K. Maslov, H. Yang, Q. Zhou, K. Shung, and L. V. Wang, "Photoacoustic endoscopy," *Opt. Lett.* **34**, 1591–1593 (2009).

[33] J. Yang, C. Favazza, R. Chen, J. Yao, X. Cai, K. Maslov, Q. Zhou, K. Shung, and L. V. Wang, "Simultaneous functional photoacoustic and ultrasonic endoscopy of internal organs *in vivo*," *Nat. Med.* **18**, 1297–1302 (2012).

[34] J. Yang, R. Chen, C. Favazza, J. Yao, C. Li, Z. Hu, Q. Zhou, K. Shung, and L. V. Wang, "A 2.5-mm diameter probe for photoacoustic and ultrasonic endoscopy," *Opt. Express*. **20**, 23944–23953 (2012).

[35] J. Yao, K. Maslov, Y. Zhang, Y. Xia, and L. V. Wang, "Label-free oxygen-metabolic photoacoustic microscopy *in vivo*," *J. Biomed. Opt.* **16**, 076003 (2011).

[36] J. Yao, J. Xia, K. Maslov, M. Nasiriavanaki, V. Tsytsarev, A. V. Demchenko, and L. V. Wang, "Noninvasive photoacoustic computed tomography of mouse brain metabolism *in vivo*," *Neuroimage*. **64**, 257–266 (2013).

[37] B. Wang, A. Karpiouk, D. Yeager, J. Amirian, S. Litovsky, R. Smalling, and S. Emelianov, "Intravascular photoacoustic imaging of lipid in atherosclerotic plaques in the presence of luminal blood," *Opt. Lett.* **37**, 1244–1246 (2012).

[38] M. A. Yaseen, S. A. Ermilov, H. Brecht, R. Su, A. Conjusteau, M. Fronheiser, B. A. Bell, M. Motamedi, and A. A. Oraevsky, "Optoacoustic imaging of the prostate: development toward image-guided biopsy," *J. Biomed. Opt.* **15**, 021310 (2013).

[39] R. H. Hawes and P. Fockens, *Endosonography*, 4th ed. (Elsevier, 2018).

[40] L. Wang, K. Maslov, J. Yao, B. Rao, and L. V. Wang, "Fast voice-coil scanning optical-resolution photoacoustic microscopy," *Opt. Lett.* **36**, 139–141 (2011).

[41] C. Li, J. Yang, R. Chen, C. Yeh, L. Zhu, K. Maslov, Q. Zhou, K. K. Shung, and L. V. Wang, " Urogenital photoacoustic endoscope," *Opt. Lett.* **39**, 1473–1476 (2014).

[42] Y. Park, J. Kim, C. Lee, S. Jeon, G. Lim, and C. Kim, "Handheld Photoacoustic Microscopy Probe," *Sci. Rep.* **7**, 13359 (2017).

[43] M. Basij, Y. Yan, S. S. Alshahrani, H. Helmi, T. K. Burton, J. W. Burmeister, M. M. Dominello, I. S. Winer, and M. Mehrmohammadi, " Miniaturized phased-array ultrasound and photoacoustic endoscopic imaging system," *Photoacoustics*, **15**, 100139 (2019).

[44] D. N. Danforth, “The morphology of the human cervix,” *Clin. Obstet. Gynecol.* **26**, 7–13 (1983).

[45] M. S. Mahendroo, A. Porter, D. W. Russell, and R. A. Word, "The Parturition defect in steroid 5α-reductase type 1 knockout mice is due to impaired cervical ripening," *Mol. Endocrinol.* **13**, 981–992 (1999).

[46] T. Rechberger, S. R. Abramson, and J. F. Woessner, "Onapristone and prostaglandin E2 induction of delivery in the rat in late pregnancy: a model for the analysis of cervical softening," *Am. J. Obstet. Gynecol.* **175**, 719–723 (1996).

[47] B. Timmons, M. Akins, and M. Mahendroo, "Cervical remodeling during pregnancy and parturition," *Trends Endocrinol. Metab.* **21**, 353–361 (2010).

[48] J. R. Challis, C. J. Lockwood, L. Myatt, J. E. Norman, J. F. Strauss III, and F. Petraglia, "Inflammation and pregnancy," *Reprod. Sci.* **16**, 206–215 (2009).

[49] J. Anderson, N. Brown, M. S. Mahendroo, and J. Reese, "Utilization of different aquaporin water channels in the mouse cervix during pregnancy and parturition and in models of preterm and delayed cervical ripening," *Endocrinology* **147**, 130–140 (2006).

[50] V. N. A. Breeveld-Dwarkasing, J.M. te Koppele, R.A. Bank, G.C. van der Weijden, M.A.M. Taverne, and F.M.F. van Dissel-Emiliani, "Changes in water content, collagen degradation, collagen content, and concentration in repeated biopsies of the cervix of pregnant cows," *Biol. Reprod.* **69**, 1608–1614 (2003).

[51] D. A. Burns and E. W. Ciurczak, *Handbook of Near-Infrared Analysis*, 3rd ed. (Taylor & Francis, 2008).

[52] K. Suehara, Y. Ohta, Y. Nakano, and T. Yano, "Rapid measurement and control of the moisture content of compost using near-infrared spectroscopy," *J. Biosci. Bioeng.* **87**, 769–774 (1999).

[53] Z. Xu, C. Li, and L. V. Wang, “Photoacoustic tomography of water in phantoms and tissue,” *J. Biomed. Opt.* **15**, 036019 (2010).

[54] B. Cox, J. G. Laufer, P. C. Beard, S. R. Arridge, “Quantitative spectroscopic photoacoustic imaging: a review,” *J. Biomed. Opt.* **17**, 061202 (2012).

[55] T. J. Allen, P. C. Beard, A. Hall, A. P. Dhillon, and J. S. Owen, “Spectroscopic photoacoustic imaging of lipid-rich plaques in the human aorta in the 740 to 1400 nm wavelength range,” *J. Biomed. Opt.* **17**, 061209 (2012).

[56] P. Wang, J. R. Rajian, and J. Cheng, “Spectroscopic imaging of deep tissue through photoacoustic detection of molecular vibration,” *J. Phys. Chem. Lett.* **4**, 2177–2185 (2013).

[57] J. Yang, C. Li, R. Chen, Q. Zhou, K. K. Shung, and L. V. Wang, “Catheter-based photoacoustic endoscope,” J. Biomed. Opt. 19, 066001 (2014).

[58] J. Yang, C. Li, R. Chen, B. Rao, J. Yao, C. Yeh, A. Danielli, K. Maslov, Q. Zhou, K. K. Shung, and L. V. Wang, “Optical-resolution photoacoustic endomicroscopy *in vivo*,” *Biomed. Opt. Express* **6**, 918–932 (2015).

[59] G. D. Ludwig, "The Velocity of Sound through Tissues and the Acoustic Impedance of Tissues," *Journal of the Acoustical Society of America*, **22**, 862-866 (1950).

[60] L. B. Koralov and Y. G. Sinai, *Theory of probability and random processes*, 2nd edition (Springer, 2007).

[61] M. W. Tibbitt and K. S. Anseth, “Hydrogels as extracellular matrix mimics for 3D cell culture,” *Biotechnol. Bioeng*. **103**, 655–663 (2009).

[62] N. Gjorevski, N. Sachs, A. Manfrin, S. Giger, M. E. Bragina1, P. Ordóñez-Morán, H. Clevers, and M. P. Lutolf, “Designer matrices for intestinal stem cell and organoid culture,” *Nature* **539**, 560–564 (2016).

[63] T. Takezawa, K. Ozaki, A. Nitani, C. Takabayashi, and T. Shimo-Oka, "Collagen vitrigel: a novel scaffold that can facilitate a three-dimensional culture for reconstructing organoids," *Cell Transplant.* **13**, 463–474 (2004).

[64] F. A. Duck, *Physical Properties of Tissue: A Comprehensive Reference Book* (Academic Press, 1990).

[65] R. H. Wilson, K. P. Nadeau, F. B. Jaworski, B. J. Tromberg, and A. J. Durkin, "Review of short-wave infrared spectroscopy and imaging methods for biological tissue characterization," *J. Biomed. Opt.* **20**, 030901 (2015).

[66] R. Tuvikene, K. Truus, A. Kollist, O. Volobujeva, E. Mellikov, and T. Pehk, "Gel-forming structures and stages of red algal galactans of different sulfation levels," *J. Appl. Phycol.* **20**, 527–535 (2008).

[67] J. Laufer, C. Elwell, D. Delpy, and P. Beard, "In vitro measurements of absolute blood oxygen saturation using pulsed near-infrared photoacoustic spectroscopy: accuracy and resolution," *Phys. Med. Biol.* **50**, 4409–4428 (2005).

[68] L. V. Wang, S. L. Jacques, and L. Zheng, "MCML—Monte Carlo modeling of light transport in multi-layered tissues," *Comput. Meth. Programs Biomed.* **47**, 131–146 (1995).

[69] T. L. Troy and S. N. Thennadil, "Optical properties of human skin in the near infrared wavelength range of 1000 to 2200 nm," *J. Biomed. Opt.* **6**, 167–176 (2001).

[70] K. Myers, S. Socrate, D. Tzeranis, and M. House, "Changes in the biochemical constituents and morphologic appearance of the human cervical stroma during pregnancy," *Eur. J. Obstet. Gynecol. Reprod. Biol.* **144S**, S82–S89 (2009).

[71] A. Agresti, *Foundations of Linear and Generalized Linear Models* (Wiley, 2015).

[72] N. Rappoport, J. Toung, D. Hadley, R. J. Wong, K. Fujioka, J. Reuter, C. W. Abbott, S. Oh, D. Hu, C. Eng, S. Huntsman, D. L. Bodian, J. E. Niederhuber, X. Hong, G. Zhang, W. Sikora-Wohfeld, C. R. Gignoux, H. Wang, J. Oehlert, L. L. Jellife-Pawlowski, J. B. Gould, G. L. Darmstadt, X. Wang, C. D. Bustamante, M. P. Snyder, E. Ziv, N. A. Patsopoulos, L. J. Muglia, E. Burchard, G. M. Shaw, H. M. O'Brodovich, D. K. Stevenson, A. J. Butte, and M. Sirota, "A genome-wide association study identifies only two ancestry specific variants associated with spontaneous preterm birth," *Sci. Rep*. **8**, 226 (2018).

[73] B. J. Callahan, D. B. DiGiulio, D. S. A. Goltsman, C. L. Sun, E. K. Costello, P. Jeganathan, J. R. Biggio, R. J. Wong, M. L. Druzin, G. M. Shaw, D. K. Stevenson, S. P. Holmes, and D. A. Relman, "Replication and refinement of a vaginal microbial signature of preterm birth in two racially distinct cohorts of US women," *Proc. Natl. Acad. Sci. U. S. A.* **114**, 9966–9971 (2017).

[74] L. J. Muglia and M. Katz, "The enigma of spontaneous preterm birth," *N. Engl. J. Med.* **362**, 529–535 (2010).

[75] K. L. Downes, P. Gajer, J. Ravel, and M. A. Elovitz, "359: integrating low and high risk cervicovaginal microbiota with antimicrobial peptides may identify those women at greatest risk for spontaneous preterm birth," *Am. J. Obstet. Gynecol.* **216**, S218 (2017).

[76] I. Kononenko, "Machine learning for medical diagnosis: history, state of the art and perspective," *Artif. Intell. Med*. **23**, 89–109 (2001).

[77] R. O. Duda, P. E. Hart, and D. G. Stork, *Pattern Classification*, 2nd ed. (Wiley, 2001).

[78] C. M. O'Brien, J. L. Herington, N. Brown, I. J. Pence, B. C. Paria, J. C. Slaughter, J. Reese, and A. Mahadevan-Jansen, "*In vivo* Raman spectral analysis of impaired cervical remodeling in a mouse model of delayed parturition," *Sci. Rep*. **7**, 6835 (2017).

[79] C. M. O'Brien, E. Vargis, A. Rudin, J. C. Slaughter, G. Thomas, J M. Newton, J. Reese, K. A. Bennett, and A. Mahadevan-Jansen, "*In vivo* Raman spectroscopy for biochemical monitoring of the cervix throughout pregnancy," *Am. J. Obstet. Gynecol.* **218**, 528.e1–528.e18 (2018).

[80] M. L. Akins, K. Luby-Phelps, and M. Mahendroo, "Second harmonic generation imaging as a potential tool for staging pregnancy and predicting preterm birth," *J. Biomed. Opt.* **15**, 026020 (2010).

[81] Y. Zhang, M. L. Akins, K. Murari, J. Xi, M. Li, K. Luby-Phelps, M. Mahendroo, and X. Li, "A compact fiber-optic SHG scanning endomicroscope and its application to visualize cervical remodeling during pregnancy," *Proc. Natl. Acad. Sci. U. S. A*. **109**, 12878–12883 (2012).

[82] R. J. Kuon, S. Q. Shi, H. Maul, C. Sohn, J. Balducci, L. Shi, and R. E. Garfield, "A novel optical method to assess cervical changes during pregnancy and use to evaluate the effects of progestins on term and preterm labor," *Am. J. Obstet. Gynecol.* **205**, 82.e15–82.e20 (2011).

[83] M. Leslie, "Tumors' do-it-yourself blood vessels," *Science* **352**, 1381–1383 (2016).

[84] Y. He, L. Wang, J. Shi, J. Yao, L. Li, R. Zhang, C. Huang, J. Zou, and L. V. Wang, "*In vivo* label-free photoacoustic flow cytography and on-the-spot laser killing of single circulating melanoma cells," *Sci. Rep.* **6**, 39616 (2016).

[85] P. Carmeliet and R. K. Jain, "Molecular mechanisms and clinical applications of angiogenesis," *Nature* **473**, 298–307 (2011).

[86] S. Sharma, M. C. Sharma, and C. Sarkar, "Morphology of angiogenesis in human cancer: a conceptual overview, histoprognostic perspective and significance of neoangiogenesis," *Histopathology* **46**, 481–489 (2005).

[87] E. Crowley, F. Di Nicolantonio, F. Loupakis, and A. Bardelli, “Liquid biopsy: monitoring cancer-genetics in the blood,” *Nat. Rev. Clin. Oncol*. **10**, 472–484 (2013).

[88] D. M. McDonald and P. L. Choyke, “Imaging of angiogenesis: from microscope to clinic,” *Nat. Med.* **9**, 713–725 (2003).

[89] L. Lin, P. Zhang, S. Xu, J. Shi, L. Li, J. Yao, L. Wang, J. Zou, and L. V. Wang, “Handheld optical-resolution photoacoustic microscopy,” *J. Biomed. Opt*. **22**, 041002 (2017).

[90] M. Strathman, Y. Liu, E. G. Keeler, M. Song, U. Baran, J. Xi, M. Sun, R. Wang, X. Li, and L. Y. Lin, “MEMS scanning micromirror for optical coherence tomography,” *Biomed. Opt. Express* **6**, 211–224 (2015).

[91] J. Yao, C. H. Huang, L. Wang, J. M. Yang, L. Gao, K. Maslov, J. Zou, and L. V. Wang, “Wide-field fast-scanning photoacoustic microscopy based on a water-immersible MEMS scanning mirror,” *J. Biomed. Opt.* **17**, 080505 (2012).

[92] R. A. Word, X. Li, M. Hnat, and K. Carrick, “Dynamics of cervical remodeling during pregnancy and parturition: mechanisms and current concept,” *Sem. Reprod. Med.* **25**, 69–79 (2007).

[93] Y. Liang, L. Jin, B. Guan, and L. Wang, “2 MHz multi-wavelength pulsed laser for functional photoacoustic microscopy,” *Opt. Lett.* **42**, 1452–1455 (2017).

[94] K. Yu, C. Zhang, G. J. Berry, R. B. Altman, C. Re´, D. L. Rubin, and M. Snyder, “Predicting non-small cell lung cancer prognosis by fully automated microscopic pathology image features,” *Nat. Commun.* **7**, 12474 (2016).

[95] A. Esteva, B. Kuprel, R. A. Novoa, J. Ko, S. M. Swetter, H. M. Blau, and S. Thrun, “Dermatologist-level classification of skin cancer with deep neural networks,” *Nature* **542**, 115–118 (2017).

[96] L. Liu, S. Oza, D. Hogan, Y. Chu, J. Perin, J. Zhu, J. E. Lawn, S. Cousens, C. Mathers, and R. E. Black, "Global, regional, and national causes of under-5 mortality in 2000-15: an updated systematic analysis with implications for the Sustainable Development Goals," *Lancet* **388**, 3027-3035 (2016).

[97] R. Romero, S. K. Dey, and S. J. Fisher, “Preterm labor: one syndrome, many causes,” *Science* **345**, 760–765 (2014).

[98] H. F. Zhang, K. Maslov, M. Sivaramakrishnan, G. Stoica, and L. V. Wang, “Imaging of hemoglobin oxygen saturation variations in single vessels in vivo using photoacoustic microscopy,” *Appl. Phys. Lett.* **90**, 053901–765 (2007).

[99] W. Montagna and K. Carlisle, “The architecture of black and white facial skin,” *Journal of the American Academy of Dermatology* **24**, 929–937 (1991).

[100] M. J. C. Van Gemert, S. L. Jacques, H. J. C. M. Sterenborg, and W. M. Star, “Skin optics,” *IEEE Transactions on Biomedical Engineering* **36**, 1146–1154 (1989).

[101] H. Büning-Pfaue, " Analysis of water in food by near infrared spectroscopy," *Food Chem.* **82**, 107-115 (2003).

[102] Y. Wang, W. Wen, K. Wang, P. Zhai., P. Qiu, and K. Wang, " Measurement of absorption spectrum of deuterium oxide (D2O) and its application to signal enhancement in multiphoton microscopy at the 1700-nm window," *Appl. Phys. Lett.* **108**, 021112 (2016)

[103] S. H. Strogatz, *Nonlinear Dynamics and Chaos: With Applications to Physics, Biology, Chemistry, and Engineering*, 2nd edition (CRC Press, 2015).

[104] R. W. Bourdeau, A. Lee-Gosselin, A. Lakshmanan, A. Farhadi, S. R. Kumar, S. P. Nety, and M. G. Shapiro, "Acoustic reporter genes for noninvasive imaging of microorganisms in mammalian hosts," *Nature* **553**, 86–90 (2018).

[105] A. Lev-Sagie, D. Goldman-Wohl, Y. Cohen, M. Dori-Bachash, A. Leshem, U. Mor, J. Strahilevitz, A. E. Moses, H. Shapiro, S. Yagel, and E. Elinav, "Vaginal microbiome transplantation in women with intractable bacterial vaginosis," *Nature Medicine* **25**, 1500–1504 (2019).

[106] J. Shi, T. T. W. Wong, Y. He, L. Li, R. Zhang, C. S. Yung, J. Hwang, K. Maslov, and L. V. Wang, " High-resolution, high-contrast mid-infrared imaging of fresh biological samples with ultraviolet-localized photoacoustic microscopy," *Nature Photonics* **13**, 609–615 (2019).

[107] Y. Qu, L. Li, Y. Shen, X. Wei, T. T. W. Wong, P. Hu, J. Yao, K. Maslov, and L. V. Wang, “Dichroism-sensitive photoacoustic computed tomography,” *Optica* **5**, 495-501 (2018).

[108] Y. Qu, P. Hu, J. Shi, K. Maslov, P. Zhao, C. Li, J. Ma, A. Garcia-Uribe, K. Meyers, E. Diveley, S. Pizzella, L. Muench, N. Punyamurthy, N. Goldstein, O. Onwumere, M. Alisio, K. Meyenburg, J. Maynard, K. Helm, E. Altieri, J. Slaughter, S. Barber, T. Burger, C. Kramer, J. Chubiz, M. Anderson, R. McCarthy, S. K. England, G. A. Macones, M. J. Stout, M. Tuuli, and L. V. Wang, “In vivo characterization of connective tissue remodeling using infrared photoacoustic spectra,” *J. Biomed. Opt.* **23**, 121621 (2018).

[109] Y. Qu, C. Li, J. Shi, R. Chen, S. Xu, H. Rafsanjani, K. Maslov, H. Krigman, L. Garvey, P. Hu, P. Zhao, K. Meyers, E. Diveley, S. Pizzella, L. Muench, N. Punyamurthy, N. Goldstein, O. Onwumere, M. Alisio, K. Meyenburg, J. Maynard, K. Helm, E. Altieri, J. Slaughter, S. Barber, T. Burger, C. Kramer, J. Chubiz, M. Anderson, R. McCarthy, S. K. England, G. A. Macones, Q. Zhou, K. K. Shung, J. Zou; M. J. Stout, M. Tuuli, and L. V. Wang, “Transvaginal fast-scanning optical-resolution photoacoustic endoscopy,” *J. Biomed. Opt.* **23**, 121617 (2018).